Atom Interferometric Inertial Sensors for Space Applications

Philippe Bouyer[1], Franck Pereira dos Santos[2], Arnaud Landragin[2], and Christian J. Bordé[2]

[1] Laboratoire Charles Fabry de l'Institut d'Optique, CNRS, Université Paris-Sud Campus Polytechnique, RD127
91127 Palaiseau cedex, France
[2] LNE-SYRTE, UMR8630, Observatoire de Paris, 61 avenue de l'Observatoire, 75014 Paris, France
philippe.bouyer@iota.u-psud.fr http://atomoptic.fr

Summary. The techniques of atom cooling combined with atom interferometry make possible the realisation of very sensitive and accurate inertial sensors like gyroscopes or accelerometers. Besides earth-based developments, the use of these techniques in space should provide extremely high sensitivity for research in fundamental physics.

1 Introduction

Inertial sensors are useful devices in both science and industry. Higher precision sensors could find scientific applications in the areas of general relativity [1], geodesy and geology. There are also important applications of such devices in the field of navigation, surveying and analysis of earth structures. Matter-wave interferometry was envisaged for its potential to be an extremely sensitive probe for inertial forces [2]. First, neutron interferometers have been used to measure the acceleration due to gravity [3] and the rotation of the Earth [4] at the end of the seventies. In 1991, atom interference techniques [5, 31] have been used in proof-of-principle work to measure rotations [6] and accelerations [7]. In the following years, many theoretical and experimental works have been performed to investigate this new kind of inertial sensors [8]. Some of the recent works have shown very promising results leading to a sensitivity comparable to other kinds of sensors, for rotation [9,10] as well as for acceleration [11, 12].

Atom interferometry [2, 6, 8, 13, 14] is nowadays one of the most promising candidates for ultra-precise and ultra-accurate measurement of gravito-inertial forces [9–12, 15–17] or for precision measurements of fundamental constants [18]. The realisation of Bose–Einstein condensation (BEC) of a dilute gas of

trapped atoms in a single quantum state [19–21] has produced the matter-wave analog of a laser in optics [22–25]. Alike the revolution brought by lasers in optical interferometry [1,26,27], it is expected that the use of Bose–Einstein condensed atoms will bring the science of atom optics, and in particular atom interferometry, to an unprecedented level of accuracy [28, 29]. In addition, BEC-based coherent atom interferometry would reach its full potential in space-based applications where micro-gravity will allow the atomic interferometers to reach their best performance [30].

2 Inertial Sensors Based on Atom Interferometry: Basic Principle

Generally, atom interferometry is performed by applying successive *coherent* phase-locked beam-splitting processes separated by a time T to an ensemble of particles (see Fig. 1) [31,32], followed by detection of the particles in each of the two output channels. The interpretation in terms of matter waves follows from the analogy with optical interferometry. The incoming matter wave is separated into two different paths by the first beam splitter. The accumulation of phases along the two paths leads to interference at the last beam splitter, producing complementary probability amplitudes in the two output channels [33–35]. The detection probability in each channel is then a sine function of the accumulated phase difference, $\Delta\phi$.

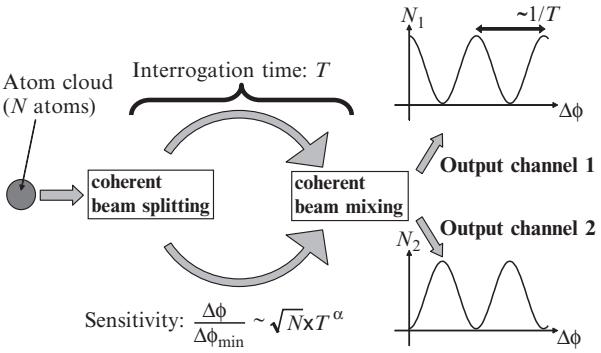

Fig. 1. Principle of an atom interferometer. An initial atomic wave packet is split into two parts by the first beam splitter. The wave packets then propagate freely along the two different paths for an "interrogation time" T, during which the two wave packets can accumulate different phases. A second pulse is then applied to the wave packets so that the number of atoms at each output is modulated with respect to this phase difference. The maximum sensitivity achievable for such an apparatus can be defined by comparing the variation of the number of atoms ΔN due to the phase difference $\Delta\phi$ at the output ($\Delta N \sim N\Delta\phi/2\pi \propto NT^{\alpha}$) with the quantum projection noise arising from atom counting $\sqrt{N}$. It scales as $\sqrt{N} \times T^{\alpha}$.

Atomic clocks [36–38] can be considered one of the most advanced application of atom interferometry [39]. In this "interferometer", the two different paths of Fig. 1 consist of the free evolution of atoms in different internal states with an energy separation $\hbar\omega_{at}$. An absolute standard of frequency is obtained by servo-locking a local oscillator to the output signal of the interferometer. The output signal of the clock then varies as $\cos(\Delta\omega \times T)$ where $\Delta\omega$ is the frequency difference between the transition frequency ω_{at} and the local oscillator frequency ω. Atom interferometers can also be used as a probe of gravito-inertial fields. In such applications, the beam splitters usually consist of pulsed near-resonance light fields which interact with the atoms to create a coherent superposition of two different *external* degrees of freedom, by coherent transfer of momentum from the light field to the atoms [2, 5, 31]. Consequently, the two interferometer paths are separated in space, and a change in the gravito-inertial field in either path will result in a modification of the accumulated phase difference. Effects of acceleration and rotation can thus be measured with very high accuracy. To date, ground-based experiments using atomic gravimeters (measuring acceleration) [11, 40], gravity gradiometers (measuring acceleration gradients) [15, 41] and gyroscopes [9, 10] have been realised and proved to be competitive with existing optical [42] or artefact-based devices [43].

3 Atom Interferometers Using Light Pulses as *Atom-Optical* Elements

The most developed atom interferometer inertial sensors are today atomic state interferometers [31, 48] which in addition use two-photon velocity selective Raman transitions [44, 45] to manipulate atoms while keeping them in long-lived ground states. With the Raman excitation, two laser beams of frequency ω_1 and ω_2 are tuned to be nearly resonant with an allowed optical transition. Their frequency difference $\omega_1 - \omega_2$ is chosen to be resonant with a microwave transition between two atomic ground-state levels. Under appropriate conditions, the atomic population Rabi flops between the ground-state levels with a rate proportional to the product of the two single-photon Rabi frequencies and inversely proportional to the optical detuning. When the beams are aligned to counter-propagate, a momentum exchange of approximately twice the single-photon momentum accompanies these transitions. This leads to a strong Doppler sensitivity of the two-photon transition frequency, and can be used to coherently divide (with a $\pi/2$ pulse) or deflect (with a π pulse) atomic wave packets. (On the other hand, when the beams are aligned to co-propagate, these transitions have a negligible effect on the atomic momentum, and the transition frequency is almost Doppler insensitive.)

Usually, an interferometer is formed using a $\pi/2 - \pi - \pi/2$ pulse sequence to coherently divide,[1] deflect and finally recombine an atomic wave packet (as in a Mach–Zehnder interferometer in optics). The resulting interference can be directly observed by measuring the atomic ground-state populations [13]. In comparison with mechanical nano-fabricated gratings [14], optical gratings can be easily vibrationally isolated from the vacuum chamber [46]. Scattering from standing waves [32, 47] can be efficient and capable of large momentum transfer. However, these beam splitters typically require a highly collimated atomic beam. In contrast, the stimulated Raman transition linewidth can be adjusted to address large transverse velocity spreads, relaxing collimation requirements and increasing interferometer count rates.

We present in this section a summary of recent work with light-pulse interferometer-based inertial sensors. We first outline the general principles of operation of light-pulse interferometers. This atomic interferometer [31, 48] uses two-photon velocity selective Raman transitions [44], to manipulate atoms while keeping them in long-lived ground states.

3.1 Principle of Light-Pulse Matter-Wave Interferometers

Light-pulse interferometers work on the principle that, when an atom absorbs or emits a photon, momentum must be conserved between the atom and the light field. Consequently, an atom which emits (absorbs) a photon of momentum $\hbar\boldsymbol{k}$ will receive a momentum impulse of $\Delta\boldsymbol{p} = -\hbar\boldsymbol{k}(+\hbar\boldsymbol{k})$. When a resonant travelling wave is used to excite the atom, the internal state of the atom becomes correlated with its momentum: an atom in its ground state $|1\rangle$ with momentum $\boldsymbol{p}$ (labelled $|1, \boldsymbol{p}\rangle$) is coupled to an excited state $|2\rangle$ of momentum $\boldsymbol{p} + \hbar\boldsymbol{k}$ (labelled $|2, \boldsymbol{p} + \hbar\boldsymbol{k}\rangle$) [31, 48]. A precise control of the light-pulse duration allows a complete transfer from one state (for example $|1, \boldsymbol{p}\rangle$) to the other ($|2, p + \hbar\boldsymbol{k}\rangle$) in the case of a π pulse and a 50/50 splitting between the two states in the case of a $\pi/2$ pulse (half the area of a π pulse). This is analogous to a polarising beam splitter (PBS) in optics, where each output port of the PBS (i.e. the photon momentum) is correlated to the laser polarisation (i.e. the photon state). In the optical case, a precise control of the input beam polarisation adjusts the balance between the output ports. In the case of atoms, a precise control of the light-pulse duration plays the role of the polarisation control.

In the $\pi/2 - \pi - \pi/2$ configuration, the first $\pi/2$ pulse excites an atom initially in the $|1, \boldsymbol{p}\rangle$ state into a coherent superposition of states $|1, \boldsymbol{p}\rangle$ and $|2, \boldsymbol{p} + \hbar\boldsymbol{k}\rangle$. If state $|2\rangle$ is stable against spontaneous decay, the two parts of the wave packet will drift apart by a distance $\hbar kT/m$ in time T. Each partial wave packet is redirected by a π pulse which induces the transitions

[1] There are other possible configurations, such as the Ramsey–Bordé $\pi/2 - \pi/2 - \pi/2 - \pi/2$ [6] which can be extended to include multiple intermediate π pulses [8] or adiabatic transfers [49] to increase the area.

$|1, \boldsymbol{p}\rangle \rightarrow |2, \boldsymbol{p} + \hbar\boldsymbol{k}\rangle$ and $|2, \boldsymbol{p} + \hbar\boldsymbol{k}\rangle \rightarrow |1, \boldsymbol{p}\rangle$. After another interval T the two partial wave packets overlap again. A final pulse causes the two wave packets to recombine and interfere. The interference is detected by measuring, for example, the number of atoms in state $|2\rangle$. We obtain a large wave packet separation by using laser-cooled atoms and velocity selective stimulated Raman transitions [44]. A very important point of these light-pulse interferometers is their intrinsic accuracy, thanks to the knowledge of the light frequency which defines the scaling factor of the interferometers.

3.2 Application to Earth-Based Inertial Sensors

Inertial forces manifest themselves by changing the relative phase of the de Broglie matter waves with respect to the phase of the driving light field, which is anchored to the local reference frame. The physical manifestation of the phase shift is a change in the probability to find the atoms, for example, in state $|2\rangle$, after the interferometer pulse sequence described above. A complete analytic treatment of wave packet phase shifts in the case of acceleration, gradient of acceleration and rotation together [34, 39, 50–52] can be realised with the ABCDξ formalism, a formalism generalising to matter waves the ABCD matrices for light optics. In these calculations, it is always important to remember that the external fields act not only on the atoms but also on other components of the experiments, such as mirrors and laser beams and that additional contributions may enter in the final expression of the phase (the final phase expression should be independent of the gauge [39,52]). As an example, the gravitational phase shift, that can be calculated to first order using the gravitational field action integral on the atomic wave packets [31, 33, 35, 48], can be removed from the general expression of the interferometer phase shift by a simple coordinate transformation. It will then reappear in the beam-splitter phases.

The phase shift calculation obtained by an action integral along the unperturbed trajectory of the atoms works only to first order. The exact expression of the phase involves the sum of three contributions: the first one comes from the beam splitters, the second from the action integral along both paths and the third from the interferometer end points splitting under the influence of the perturbing field. When the action is calculated along the perturbed trajectories, for equal masses, one can show that it cancels for the most part with the end points splitting contribution [34, 39, 51–53], leaving the beam-splitter contribution alone with recoil correction terms. This beam-splitter contribution is a scalar product, hence invariant in coordinate transformations. If masses are unequal, the action integral produces an additional clock term which is the product of the mass difference by the mean proper time along both arms.

If the three light pulses of the pulse sequence are separated only in time, and not separated in space (usually if the velocity of the atoms is parallel to the laser beams), the interferometer is in an accelerometer (or gravimeter)

configuration. In a uniformly accelerating frame with the atoms, the frequency of the driving laser changes linearly with time at the rate of $-\boldsymbol{k}\cdot\boldsymbol{a}$. The phase shift arises from the interaction between the light and the atoms [8,34,52] and can be written:

$$\Delta\phi = \phi_1(t_1) - 2\phi_2(t_2) + \phi_3(t_3) \tag{1}$$

where $\phi_i(t_i)$ is the phase of light pulse i at time t_i relative to the atoms. If the laser beams are vertical, the gravitationally induced chirp can be written to first order[2] in g:

$$\Delta\phi_{\mathrm{acc}} = -\boldsymbol{k}\cdot\boldsymbol{g}\ T^2 \tag{2}$$

It is important to note that the phase shift $\Delta\phi$ can be calculated in a more general relativistic framework [8, 54, 55], in which the atomic fields are second quantized. The starting point is the use of coupled field equations for atomic fields of a given spin in curved space–time: e.g. coupled Klein–Gordon, Dirac or Proca equations. Gravitation is described by the metric tensor $g_{\mu\nu} = \eta_{\mu\nu} + h_{\mu\nu}$ and by tetrads, which enter in these equations. By considering $h_{\mu\nu}$ as a spin-two tensor field in flat space–time [56–58] and using ordinary relativistic quantum field theory, it is possible to derive field equations that display all interesting terms coupling Dirac atomic fields, gravitational and electromagnetic fields and simple expressions of the corresponding relativistic phase shifts in atom interferometers [54]. The terms involving h_{00} lead to the gravitational shift ($h_{00} = 2\boldsymbol{g}\cdot\boldsymbol{r}/c^2$), to shifts involving higher derivatives of the gravitational potential and to the analogue of the Thomas precession (spin–orbit coupling corrected by the Thomas factor). The gravitational phase shift (2) can then be seen as the flux of a gravito-electric field $-c^2\boldsymbol{\nabla}h_{00}/2 = \boldsymbol{g}$ through the interferometer space–time area divided by a quantum of flux $\hbar/M$ in analogy with electromagnetism. It should be noted that this phase shift does not depend on the initial atomic velocity or on the mass of the particle (this is a direct consequence of the equivalence principle).

Recently, an atomic gravimeter with accuracy comparable to the best corner cube device (FG5) has been achieved [12] (Fig. 2). The main limitation of this kind of gravimeter on earth is due to spurious acceleration from the reference platform. Measuring gravity gradient may allow to overcome this problem. Indeed, using the same reference platform for two independent gravimeters enables to extract gravity fluctuations. Such an apparatus [41], using two gravimeters as described above but sharing the same light pulses, has shown a sensitivity of $3\cdot10^{-8}\,\mathrm{s}^{-2}\,\mathrm{Hz}^{-1/2}$ and has a potential on Earth as good as $10^{-9}\,\mathrm{s}^{-2}\,\mathrm{Hz}^{-1/2}$.

[2] A detailed calculation of the complete phase shifts can be found in [51]. Equation (1) can be simply written $\Delta\phi = -k[(z_3^{\mathrm{down}} + z_3^{\mathrm{up}})/2 - z_2^{\mathrm{down}} - z_2^{\mathrm{up}} + z_1^{\mathrm{down}}]$, where z_i^{down} and z_i^{up} represent the intersection of the wave packet classical trajectory with the ith light pulse. The notation $^{\mathrm{down}}$ and $^{\mathrm{up}}$ are related to the upper and lower trajectories as depicted in Fig. 1.

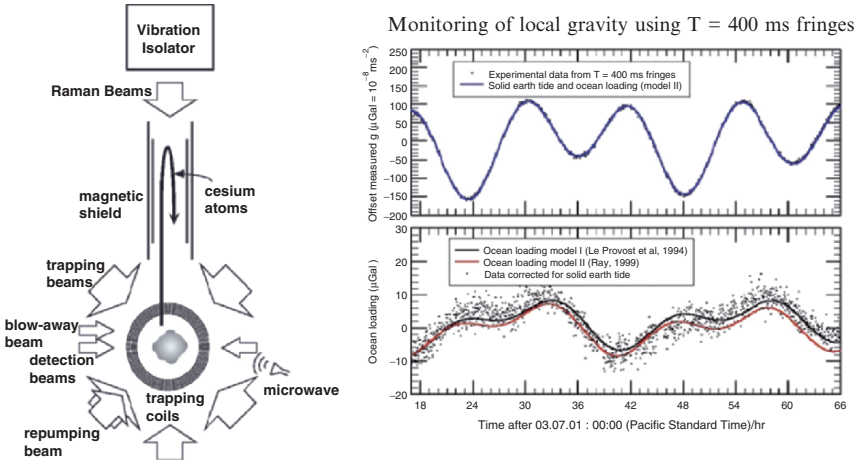

Fig. 2. Principle of the atom fountain-based gravimeter achieved in S. Chu group at Stanford. The *right figure* shows a 2 days recording of the variation of gravity. The accuracy enables to resolve ocean loading effects.

In the case of a spatial separation of the laser beams (usually if the atomic velocity is perpendicular to the direction of the laser beams), the interferometer is in a configuration similar to the optical Mach–Zehnder interferometers. Then, the interferometer is also sensitive to rotations, as in the Sagnac geometry [59] for light interferometers. For a Sagnac loop enclosing an area $\boldsymbol{A}$, a rotation $\boldsymbol{\Omega}$ produces a phase shift to first order[3] in Ω:

$$\Delta\phi_{\mathrm{rot}} = \frac{4\pi}{\lambda v_L}\,\boldsymbol{\Omega}\cdot\boldsymbol{A} \tag{3}$$

where λ is the particle wavelength and v_L its longitudinal velocity. The area A of the interferometer depends on the distance L covered between two pulses and on the recoil velocity $v_T = \hbar k/m$:

$$A = L^2\frac{v_T}{v_L} \tag{4}$$

In the general relativistic frame, (3) corresponds to the flux of a gravitomagnetic field $c^2\boldsymbol{\nabla}\times\boldsymbol{h} = 2c\boldsymbol{\Omega}$ through an area in space $\boldsymbol{A}$ divided by a quantum of flux $\hbar c/M$. The terms that involve $\boldsymbol{h} = \{h^{0k}\}$ give the Sagnac effect in a rotating frame, the spin-rotation coupling and a relativistic correction (analogous to the Thomas precession term for h_{00}). They also describe the Lense–Thirring effects from inertial frame dragging by a massive rotating body, which is a source for $\boldsymbol{h}$.

Thanks to the use of massive particles, atomic interferometers can achieve a very high sensitivity. An atomic gyroscope [10] using thermal caesium atomic beams (where the most probable velocity is $v_L \sim 300\,\mathrm{m\,s^{-1}}$) and with an

[3] A complete calculation can be found in [39].

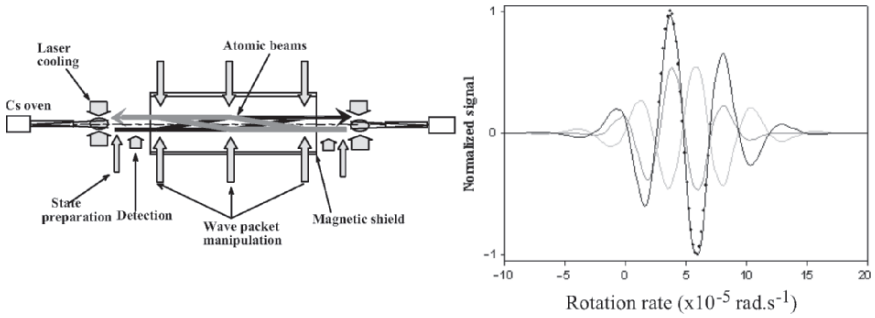

Fig. 3. Schematic diagram of the atomic Sagnac interferometer built at Yale [10]. Individual signals from the outputs of the two interferometers (*grey lines*), and difference of the two signals corresponding to a pure rotation signal (*black line*) vs. rotation rate.

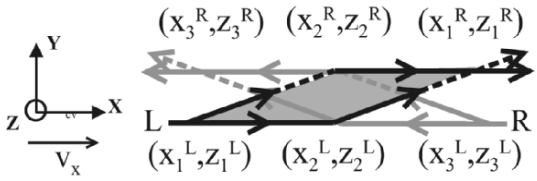

Fig. 4. General scheme of the two contra-propagating atomic interferometers. The atoms from the *left* (interferometer L) are launched with a velocity $\mathbf{v}_L = \{v_x, 0, v_z\}$ and the atoms from the *right* (interferometer R) with a velocity $\mathbf{v}_R = \{-v_x, 0, v_z\}$. They interact with the Raman beams at time t_i at position $\mathbf{r}_{i=1,2,3}^{L,R}$, respectively.

overall interferometer length of 2 m has demonstrated a sensitivity (Fig. 3) of $6 \cdot 10^{-10}\,\mathrm{rad\,s^{-1}\,Hz^{-1/2}}$. The apparatus consists of a double interferometer using two counter-propagating sources of atoms, sharing the same lasers. The use of the two signals enables to discriminate between rotation and acceleration.

Indeed, acceleration cannot be discriminated from rotation in a single atomic beam sensor, as stated above. This limitation can be circumvented by installing a second, counter-propagating, cold atomic beam (see Fig. 4). When the two atomic beams are aligned to perfectly overlap, the area vectors for the resulting interferometer loops have opposite directions, and the corresponding rotational phase shifts $\Delta\phi_{\mathrm{rot}}$ have opposite signs while the acceleration phase shift $\Delta\phi_{\mathrm{acc}}$ remains unchanged. Consequently, taking the sum of the two sensors readouts will render the sensor sensitive to acceleration only: $\Delta\phi_+ \sim 2\Delta\phi_{\mathrm{acc}}$ while taking the difference between the phase shifts of each sensor, common mode rejects uniform accelerations so that $\Delta\phi_- \sim 2\Delta\phi_{\mathrm{rot}}$. In addition, the difference $\Delta\phi_-$ common rejects the residual geometrical phase error $\delta\Phi_{\mathrm{geo}}$ if the phase fluctuations have no temporal variation on a timescale $2T$, the interferometer time. This is not the case for $\Delta\phi_+$ where a absolute phase bias $2\delta\Phi_{\mathrm{geo}}$ appears.

4 Cold Atom Sensors

4.1 Cold Atom Accelerometers

Accelerometer

Following the pioneering work of S. Chu, M. Kasevich and coworkers (see Fig. 2), new experiments have been developed to test new gravimeter configurations [60–62] or to improve previous measurements [63, 64]. We discuss in detail here the cold atom accelerometer developed at LNE-SYRTE in Paris for the watt balance experiment [65, 141] which is currently setup in the prospect of a new definition of the mass unit. This gravimeter measures the acceleration of freely falling ^{87}Rb atoms. Here, k (used in (2)) is the effective wave vector of the Raman transition, and T is the time between the interferometer Raman pulses.

This setup uses an original frequency locking system that enables to control dynamically the frequency of the two lasers, over the whole experimental sequence. First the lasers are tuned to the frequencies required to cool ^{87}Rb atoms in a magneto-optical trap (MOT). Dividing the total available laser power between a two-dimensional MOT (2D-MOT) [66] and a three-dimensional MOT (3D-MOT), loading rates of $3 \cdot 10^9$ atoms per second are obtained. Then, the magnetic field is turned off for further cooling of the atoms. Once the atoms have been released from the molasses, a frequency ramp detunes the two vertical counter-propagating beam to a detuning Δ of up to 2 GHz from the optical transition resonance. This will allow to use both the cooling and re-pumping vertical laser beam of the MOT as the Raman laser with negligible spontaneous emission (which is a decoherence process). To be used as Raman lasers, the frequency difference between these two lasers has to be subsequently phase locked with a high-bandwidth PLL. To reach an accuracy of $10^{-9} \times g$, the phase error arising from the transient evolution of their relative phase has to remain below 0.3 mrad [63]. It takes a few hundreds µs for the lock to come perfectly to the right frequency and to start phase locking (see Fig. 5), the 0.3 mrad criterion being reached in about 2 ms. (The measured spectral phase noise density in steady state [67] corresponds to a contribution of 0.56 mrad rms of phase noise in the atomic interferometer, i.e. $10^{-9} \times g$ rms.)

The Raman detuning Δ can be changed at will and other sweeps can be added in the cycle. This enables to realise first a velocity selective Raman pulse ($\sim 35\,\mu$s), with the detuning of 2 GHz which reduces the spontaneous emission. Then the detuning is swept back by 1 GHz for the interferometer itself, to achieve a better transfer efficiency.[4] Finally, the phased-locked Raman lasers are used to realise the interferometer. Owing to the Doppler effect, the

[4] Roughly speaking, the transfer efficiency is related to the pulse duration $\tau \propto \Delta/I$ where I is the Raman laser intensity, since for smaller τ, the Raman diffraction process will be less velocity selective [45].

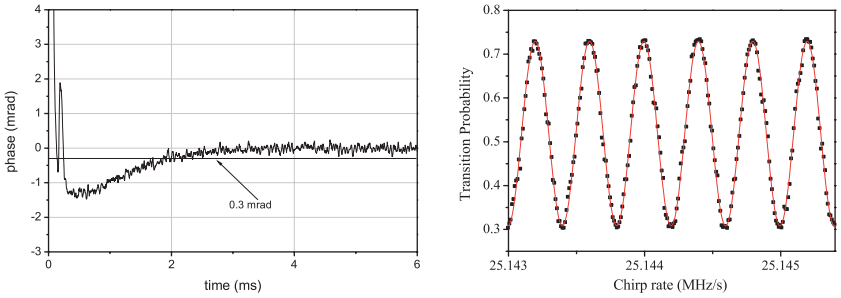

Fig. 5. *Left*: Relative Raman beams phase error. The phase lock loop (*PLL*) is closed at $t = 0$ after the 2 GHz sweep. After 0.5 ms, the phase error is exponentially decreasing with a time constant of 2 ms. *Right*: Atomic interferometer fringes obtained by scanning the Raman detuning chirp rate within the interferometer. The time between the Raman pulses is $T = 50$ ms. The *solid line* is a sinusoidal fit of the experimental points.

Raman detuning has to be chirped to compensate for the increasing vertical velocity of the atomic cloud. This chirp a, obtained by sweeping the frequency difference between the two lasers, induces an additional phase shift. The total interferometric phase is then given by: $\Delta\Phi = (kg - a)T^2$. Figure 5 displays the interferometric fringes obtained by scanning the chirp rate. In this experiment, T is 50 ms and the sensitivity is presently of $3.5 \cdot 10^{-8}$ g Hz$^{-1/2}$, limited by residual vibrations of the apparatus.

ONERA currently develops a gravimeter with cold atoms that should sustain external disturbances to make the instrument capable of being put onboard. For that, they take advantage of the abundance and the reliability of fibred components resulting from telecommunication technology. Indeed, the first limitations with the embarquability of these devices are optical: the laser sources necessarily require a good spectral quality (< 1 MHz), to be tunable near the atomic transition, operating CW with high powers (of a few tens to a few hundreds of milliwatts). The conventional techniques use lasers diode with external cavities, which makes the source sensitive to the vibrations. Moreover, the optical benches necessary to prepare the beams are generally large and hardly reducible. As shown later on in this chapter, the use of the components resulting from telecommunication technology will enable to profit from the robustness, perennity of those components and make it possible at the same time to miniaturize the optical system and to improve its reliability (Fig. 6).

Gradiometers

The measurement of the gradient of gravitational fields has important scientific and technical applications. These applications range from the measurement of G, the gravitational constant and tests of general relativity [68,69] to covert

Fig. 6. The *Girafon* gravimeter which is being constructed at ONERA, Palaiseau.

navigation, underground structure detection, oil-well logging and geodesy [70]. Initially at Stanford university in 1996, the development of a gravity gradiometer, whose operation is based on recently developed atom interference and laser manipulation techniques, has been followed by other developments for either space [71] or fundamental physics measurements [72]. A crucial aspect of every design is its intrinsic immunity to spurious accelerations.

The overall method is illustrated in Fig. 7. It uses light-pulse atom interferometer techniques [7,8,13] to measure the simultaneous acceleration of two laser-cooled ensembles of atoms. The relative acceleration of the atom clouds is measured by driving Doppler-sensitive stimulated two-photon Raman transitions [44] between atomic ground-state hyperfine levels. The geometry is chosen so that the measurement axis passes through both laser-cooled ensembles. Since the acceleration measurements are made simultaneously at both positions, many systematic measurement errors, including platform vibration, cancel as a common mode. This type of instrument is fundamentally different from current state-of-the-art instruments [73, 74]. First, the proof masses are

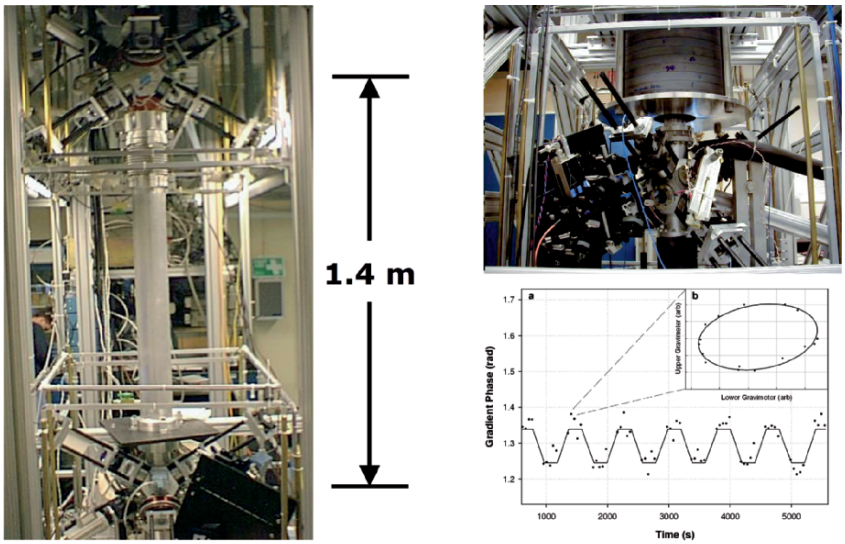

Fig. 7. Gradiometer developed in Stanford. Insert (*bottom right*), example of an application of this gradiometer to make a measurement of G [41]. A mass of 540 kg lead is alternatively brought closer to each atomic gravimeter. This preliminary measurement shows the strong potential of this system for precise measurements.

individual atoms rather than precisely machined macroscopic objects. This reduces systematic effects associated with the material properties of macroscopic objects. Second, the calibration for the two accelerometers is referenced to the wavelength of a single pair of frequency-stabilised laser beams, and is identical for both accelerometers. This provides long-term accuracy. Finally, large separations ($\gg$1 m) between accelerometers are possible. This allows for the development of high sensitivity instruments.

The relative acceleration of the two ensembles along the axis defined by the Raman beams is measured by subtracting the measured phase shifts $\Delta\phi(\boldsymbol{r}_1)$ and $\Delta\phi(\boldsymbol{r}_2)$ at each of two locations $\boldsymbol{r}_1$ and $\boldsymbol{r}_2$. The gradient is extracted by dividing the relative acceleration by the separation of the ensembles. This method determines only one component of the gravity-gradient tensor.

The Measurement of G

The Newtonian gravitational constant G is – together with the speed of light – the most popular physical constant. Introduced by Newton in 1686 to describe the gravitational force between two massive objects and first measured by Cavendish more than a hundred years later [75], G became more and more the subject of high-precision measurements. There are many motivations for such measurements [76], ranging from purely metrological interest for determinations of mass distributions of celestial objects to geophysical applications. In addition, many theoretical models profit from an accurate knowledge of G.

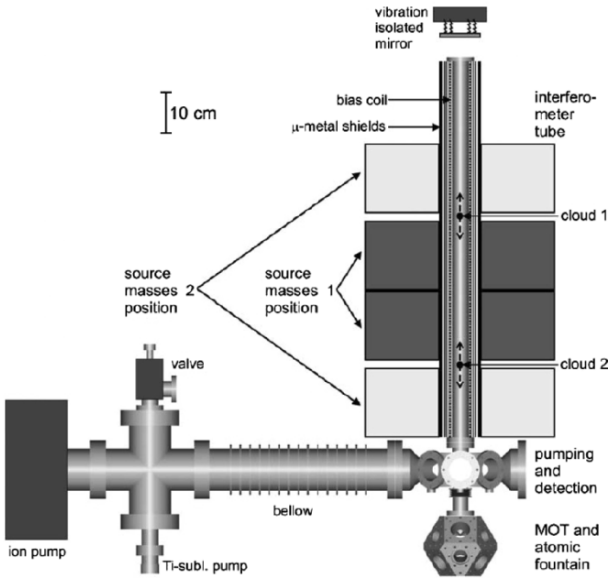

Fig. 8. Graphical illustration of the MAGIA experimental setup with the vacuum system, the atomic trajectories and the source mass positions. The laser systems, the detection units and the source mass holder are not included. The atomic trajectories during the time of the interferometer pulse sequence are sketched (*dashed arrows*).

Despite these severe motivations and some 300 measurements in the past 200 years, the 1998 CODATA [77] recommended value of $G = (6.673 \pm 0.010) \cdot 10^{11}\,\mathrm{m^3\,kg^{-1}\,s^{-2}}$ includes an uncertainty of 1,500 parts per million (ppm). Thus, G is still the least accurately known fundamental physical constant. Recently, two measurements with much smaller uncertainties of 13.7 and 41 ppm have been reported [78]. However, the given values for G still disagree on the order of 100 ppm. Therefore, it is useful to perform high resolution G measurements with different methods. This may help to identify possible systematic effects. It is worthwhile to mention that, so far, only few conceptually different methods have resulted in G measurements at the level of 1,000 ppm or better [79]. All these methods have in common that the masses, which probe the gravitational field of external source masses, are suspended (e.g. with fibres). One way to exclude this possible source of systematic effects is to perform a free-fall experiment. A high-precision measurement of G using a free-falling corner cube (FFCC) has already been performed [80] but the uncertainty remained on the order of 1,400 ppm. Experiments such as the Yale gradiometer or MAGIA developed in Italy, in which free-falling atoms are used to probe the gravitational acceleration originating from nearby source masses, are expected to surpass these results (Fig. 8).

4.2 Cold Atom Gyroscope and Cold Atom Inertial Base

Cold matter-wave gyroscopes using atomic samples with slow drift velocities of a few $\mathrm{m\,s^{-1}}$ are at present under construction at the IQ (Institut für Quantenoptik, Hannover) and have been demonstrated at LNE-SYRTE (Systèmes de Référence Temps-Espace, Paris). Both devices follow different design strategies. The cold atom sensor GOM (for Gyromètre à Onde de Matière) developed in collaboration between SYRTE and IOTA [81] is based on two caesium fountains. The two caesium ensembles are simultaneously prepared in MOTs and launched by the moving molasses technique with a speed of about $2.4\,\mathrm{m\,s^{-1}}$ and 82° in vertical direction such that they cross each other at the vertex. The interferometer is realised by applying the Raman pulses at the vertex of the atomic parabolas. The expected resolution of the setup is $4 \cdot 10^{-8}\,\mathrm{rad\,s^{-1}\,Hz^{-1/2}}$.

The cold atom Sagnac interferometer (CASI) at the IQ is based on a flat parabola design and uses intense sources of cold ^{87}Rb atoms. Figure 9 shows the vacuum chamber made out of aluminium with glued optical windows. The atomic sources on each end of the apparatus are based on a 3D-MOT loaded by a 2D-MOT. The 2D-MOT displays high performance with more than 10^{10} atoms per second. The typical loading rate of the 3D-MOT is a few 10^9 atoms per second such that 10^8 atoms can be loaded in the MOT in 0.1 s. Alternatively, the performance of the 3D-MOT can be further improved by Raman cooling in optical lattices. The actual interferometer will have a length of up

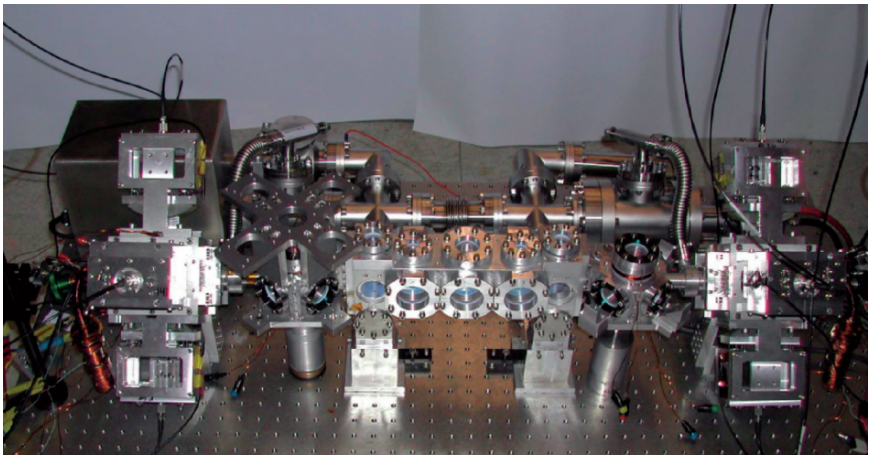

Fig. 9. The vacuum chamber of CASI. The *central part* shows the interferometry chamber with three spatially separated optical viewports for the interferometry lasers. On both sides of this chamber, a dual stage atom source is mounted which serves for the preparation of the cold atomic ensembles. The four wings on each side are the telescopes that generate elliptically shaped laser beams out of fibre-coupled lasers for cooling and trapping the Rubidium atoms.

to 15 cm. The coherent manipulation of the atoms (splitting, reflection and recombination) is performed by a temporal and/or spatially separated sequence of Raman-type interactions at the centre of the apparatus. With these parameters a shot-noise limited resolution of about $2 \cdot 10^{-9}\,\mathrm{rad\,s^{-1}\,Hz^{-1/2}}$ should be feasible using about 10^8 atoms per shot. CASI will investigate the ultimate sensitivity obtainable in cold matter-wave sensors. There is a large potential for further improvements, thanks to the expected higher stability with the use of intense cold atomic sources with a flux of more than 10^{10} atoms per second. Apart from lowering the atomic speed, the sensitivity of the apparatus can be enhanced by increasing the momentum transferred at the beam splitter as in higher-order Raman or Bragg transitions or in magneto-optical *blazed* light gratings. Their suitability for metrological applications (reproducibility, accuracy, systematic errors), however, is still to be verified. Viewing the relatively small areas achieved by present atom interferometers, an interesting alternative for such sensors may consist in waveguides (which do not deteriorate the achievable uncertainty).

The GOM is a six-axis inertial sensor. The direction of sensitivity of the setup is defined by the direction of the Raman interrogation laser with respect to the atomic trajectory. As illustrated in Fig. 10, with a classical three-pulse sequences $(\pi/2 - \pi - \pi/2)$, a sensitivity to vertical rotation Ω_z and to horizontal acceleration a_y is achieved by placing the Raman lasers horizontal and perpendicular to the atomic trajectory [9] (Fig. 10a). The same sequence, using vertical lasers, leads to the measurement of horizontal rotation Ω_y and vertical acceleration a_z (Fig. 10b). Thanks to the specific setup of the GOM, it is possible to have access to the other components of acceleration and rotation which lie along the horizontal direction of propagation of the atoms (x-axis). The use of cold atoms in strongly curved trajectories allows to point the Raman lasers along the x-direction, offering a sensitivity to acceleration a_x and no sensitivity to rotation (Fig. 10c). Easy access to the horizontal rotation Ω_x is achieved by changing the pulse sequence to four pulses: $\pi/2-\pi-\pi-\pi/2$ (Fig. 10d).

The new butterfly configuration was first proposed to measure the gravity gradient [2, 82]. It can be used to measure rotations with the same Raman beams as in the previous configuration (y-axis) but in a direction (x-axis) that cannot be achieved with a standard three-pulse sequences. Four pulses, $\pi/2 - \pi - \pi - \pi/2$, are used, separated by times $T/2 - T - T/2$, respectively. The atomic paths cross each other leading to a twisted interferometer. The horizontal projection of the oriented area cancels out so that the interferometer is insensitive to rotation around the z-axis. In contrast, the vertical projection now leads to a sensitivity to rotation around the x-axis:

$$\Delta\phi = \frac{1}{2}(\boldsymbol{k} \times (\boldsymbol{g} + \boldsymbol{a})) \cdot \boldsymbol{\Omega}\, T^3\,. \tag{5}$$

This sensitivity to rotation appears from a crossed term with acceleration $(\boldsymbol{g}+\boldsymbol{a})$ and is no longer dependent on the launching velocity. This configuration

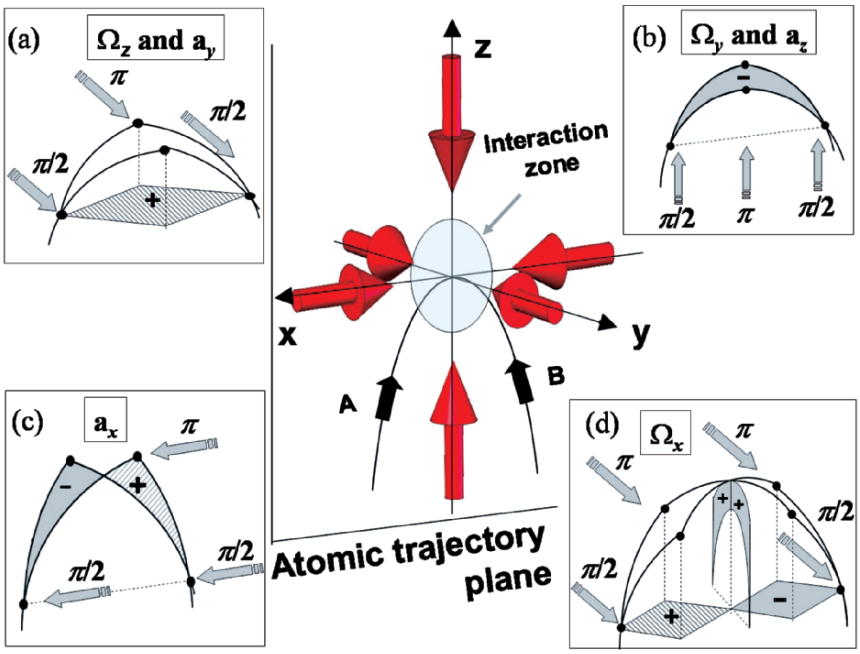

Fig. 10. Six-axis inertial sensor principle. The atomic clouds are launched on a parabolic trajectory, and interact with the Raman lasers at the top. The four configurations (**a**)–(**d**) give access to the three rotations and three accelerations. In the three pulses configuration, the Raman beams direction can be horizontal or vertical, creating the interferometer in a horizontal (**a**) or vertical (**b**, **c**) plane. With a butterfly four-pulse sequence of horizontal beams (**d**), the rotation Ω_x can be measured.

is not sensitive to DC accelerations along the direction of the Raman laser, but remains sensitive to fluctuations of horizontal and vertical accelerations. With an isolation platform, the remaining fluctuations are negligible compared to $\boldsymbol{g}$, which does not compromise the stability of the scaling factor. The sensitivity to rotation is comparable with that of configurations (a) and (b). With $2T = 60\,\mathrm{ms}$, this configuration leads to a interferometer area reduced by a factor 4.5, but it scales with T^3 and thus should present a higher sensitivity for longer interrogation times.

The atomic fringe patterns are presented in Fig. 11 and show contrasts of 4.9 and 4.2% for interferometers A and B, respectively. By operating the interferometer on the fringe side, as explained before, a signal-to-noise ratio from shot to shot of 18, limited by the residual vibrations, is achieved. The sensitivity to rotation is equal to $2.2{\cdot}10^{-5}\,\mathrm{rad\,s^{-1}}$ in 1 s, decreasing to $1.8{\cdot}10^{-6}\,\mathrm{rad\,s^{-1}}$ after 280 s of averaging time.

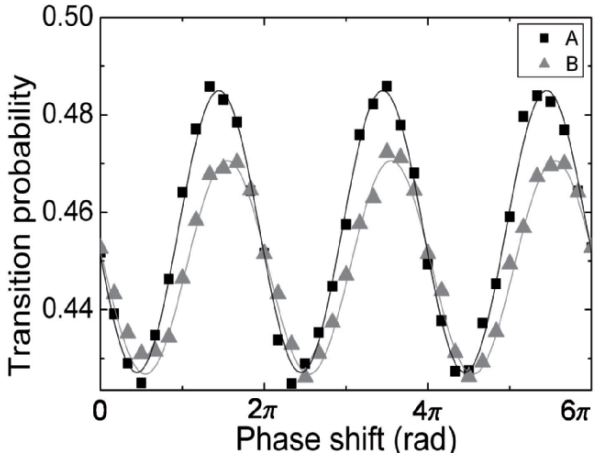

Fig. 11. Fringes obtained with both interferometers A and B in the four-pulse butterfly configuration for a total interrogation time of $2T = 60\,\mathrm{ms}$.

4.3 Ultra-Cold Sources and Applications in Space

The ultimate phase sensitivity of an atom interferometer is, aside from technical difficulties, limited by the finite number of detected particles N and scales as $\Delta\phi_{\min} = 1/\sqrt{N}$ (quantum projection noise limit [83,84]). Of course, the relation between the relative phases accumulated along the two different paths and the actual physical property to be measured is a function of the "interrogation" time T spent by the particles between the two beam splitters. Thus, the ideal sensitivity of an atom interferometer is expected to scale[5] as $\sqrt{N}\,T^{\alpha}$ with $\alpha > 0$, and it is obviously of strong interest to increase these two factors. Using cold atomic sources helps this quest for higher performances in two ways. First, a reduction of the velocity dispersion of the atomic sample (a few $\mathrm{mm\,s^{-1}}$) allows to reduce drastically the longitudinal velocity of the atoms v_L (few $\mathrm{cm\,s^{-1}}$) and enhances in the same way the enclosed area and the sensitivity for a constant length. Second, the accuracy and the knowledge of the scaling factor depend directly on the initial velocity of the atoms and can be better controlled with cold atomic sources than with thermal beams, as it has already been demonstrated with atomic clocks [85].

Nevertheless, seeking to increase the sensitivity of on-ground atom interferometers by increasing the interrogation time T, one soon reaches a limit imposed by gravity. With the stringent requirements of ultra-high vacuum and a very well-controlled environment, the current state-of-the-art in experimental realisations does not allow more than a few metres of free fall,

[5] An atomic clock or an atomic gyrometer, for example, has a sensitivity proportional to T and an on-ground gravimeter has a sensitivity proportional to T^2 due to the quadratic nature of free-fall trajectory in a constant gravitational field.

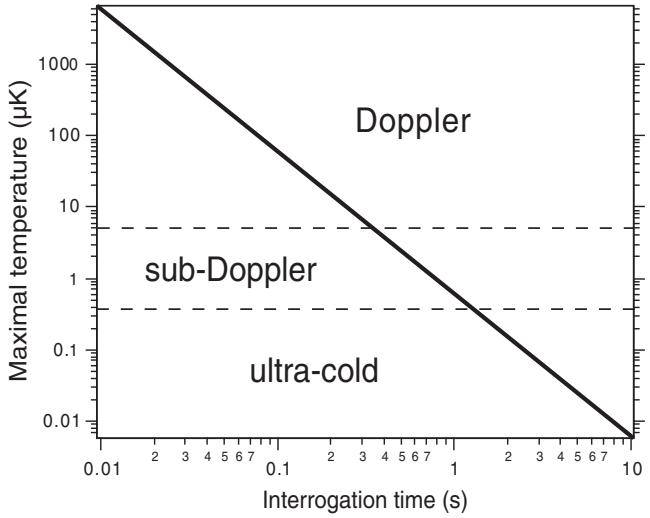

Fig. 12. Maximum temperature of atom source for a given interrogation time. The maximum interrogation time for a given initial temperature has been calculated for a detection area of $10\,\mathrm{cm}^2$ and defined as the time at which half of the atoms are no longer detected. The *dashed lines* indicate the limits of Doppler and sub-Doppler cooling. Interrogation times of several seconds are compatible only with clouds of atoms at ultra-cold temperatures, close to the quantum degenerate regime.

with corresponding interrogation times of the order of $T \sim 400\,\mathrm{ms}$. Space-based applications will allow much longer interrogation times to be used, thereby increasing dramatically the sensitivity and accuracy of atom interferometers [30].

Even in space, atom interferometry with a *classical* atomic source will not outperform the highest-precision ground-based atom interferometers that use samples of cold atoms prepared using standard techniques of Doppler and sub-Doppler laser cooling [86]. Indeed, the temperature of such sub-Doppler laser-cooled atom cloud is typically $\sim 1\,\mu\mathrm{K}$ ($v_{\mathrm{rms}} \sim 1\,\mathrm{cm\,s}^{-1}$). In the absence of gravity, the time evolution of cold samples of atoms will be dominated by the effect of finite temperature: in free space, a cloud of atoms follows a ballistic expansion until the atoms reach the walls of the apparatus where they are lost. Therefore the maximum interrogation time reasonably available for space-based atom interferometers will strongly depend on the initial temperature of the atomic source. As shown in Fig. 12, the 200 ms limit imposed by gravity for a 30 cm free fall is still compatible with typical sub-Doppler temperatures, whereas an interrogation time of several seconds is only accessible by using an "ultra-cold" source of atoms (far below the limit of laser cooling) with a temperature of the order of a few hundred nano-kelvin.

4.4 HYPER: A Proposal to Measure the Lense–Thirring Effect in Space

The HYPER project (hyper precision cold atom interferometry in space) was proposed to ESA in 2002 with the goal to benefit from the space environment, which enables very long interaction times (a few seconds) and a low spurious vibrational level. The sensitivity of the atomic interferometer is expected to reach a few $10^{-12}\,\mathrm{rad\,s^{-1}\,Hz^{-1/2}}$ for rotation and $10^{-12} \times g\,\mathrm{Hz^{-1/2}}$ for acceleration. This very sensitive and accurate apparatus offers the possibility of different tests of fundamental physics [30]. It can realise tests of general relativity by measuring the signature of the Lense–Thirring effect (magnitude and sign) or testing the equivalence principle on individual atoms. It can also be used to determine the fine structure constant by measuring the ratio of Planck's constant to an atomic mass.

The Lense–Thirring Effect

The measurement of the Lense–Thirring effect is the first scientific goal of the HYPER project and will be described in more detail in this section. The Lense–Thirring effect consists of a precession of a local inertial reference frame (realised by inertial gyroscopes) with respect to a non-local one realised by pointing the direction of fixed stars under the influence of a rotating massive body. This Lense–Thirring precession is given by

$$\boldsymbol{\Omega}_{LT} = \frac{GI}{c^2}\frac{3(\boldsymbol{\omega}\cdot\boldsymbol{r})\boldsymbol{r} - \boldsymbol{\omega}r^2}{r^5} \tag{6}$$

where G is Newton's gravitational constant, I the Earth's inertial momentum and $\boldsymbol{\omega}$ the angular velocity of the Earth. The high sensitivity of atomic Sagnac interferometers to rotation rates will enable HYPER to measure the modulation of the precession due to the Lense–Thirring effect while the satellite orbits around the Earth. In a Sun-synchronous circular orbit at 700 km altitude, HYPER will detect how the direction of the Earth's drag varies over the course of the near-polar orbit as a function of the latitudinal position θ

$$\begin{pmatrix}\Omega_x\\ \Omega_y\end{pmatrix} \propto \frac{3}{2}\begin{pmatrix}\sin(2\theta)\\ \cos(2\theta) - \frac{1}{3}\end{pmatrix}, \tag{7}$$

where e_x and e_y define the orbital plane with $\boldsymbol{e}_y$ being parallel to the Earth's inertial momentum $\boldsymbol{I}$ and $\theta \equiv \arccos(\boldsymbol{r}\cdot\boldsymbol{e}_x)$ (Fig. 13).

The HYPER Payload

HYPER carries (Fig. 14) two atomic Sagnac interferometers, each of which is sensitive to rotations around one particular axis, and a telescope used as highly sensitive star tracker (10^{-9} rad in the 0.3–3 Hz bandwidth). The two units will

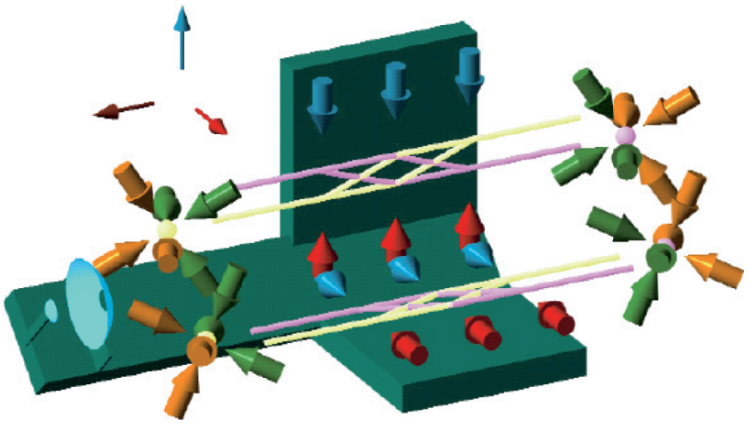

Fig. 13. Hyper gyroscopes consist of two differential atomic Sagnac interferometers in two orthogonal planes. The beam-splitting optical components are rigidly connected to the optical bench which carries the precision star tracker and serves as a non-inertial reference.

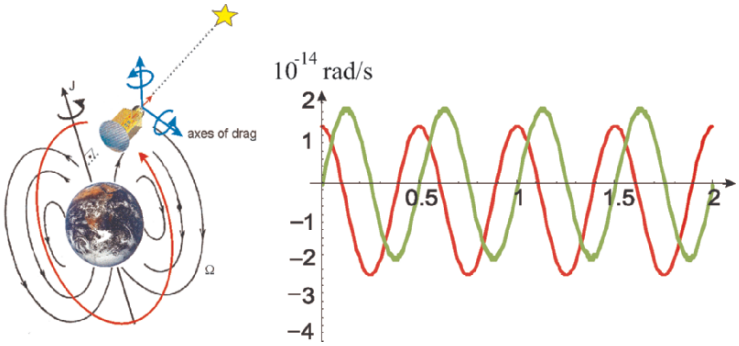

Fig. 14. Diagram of the measurement of the Lense–Thirring effect. The *black lines* visualise the vector field of the Earth's drag Ω_{LT}. The sensitive axes of the two ASUs are perpendicular to the pointing of the telescope. The direction of the Earth's drag varies over the course of the orbit showing the same structure as the field of a magnetic dipole. Due to this formal similarity, the Lense–Thirring effect is also called *gravito-magnetic effect*. The modulation of the rotation rate Ω_{LT} due to Earth's gravito-magnetism as sensed by the two orthogonal ASUs in the orbit around the Earth appears at twice the orbit frequency.

measure the vector components of the gravito-magnetic rotation rate along the two axes perpendicular to the telescope pointing direction which is directed to a guide star. The drag variation written above describes the situation for a telescope pointing in the direction perpendicular to the orbital plane of the satellite. The orbit, however, changes its orientation over the course of a year which has to be compensated by a rotation of the satellite to track continuously the guide star. Consequently the pointing of the telescope is not

always directed parallel to the normal of the orbital plane. According to the equation, the rotation rate signal will oscillate at twice the frequency of the satellite revolution around the Earth. The modulated signals have the same amplitude ($3.75 \cdot 10^{-14}\,\mathrm{rad\,s^{-1}}$) on the two axes but are in quadrature. The resolution of the atomic Sagnac units (ASU) is about $3 \cdot 10^{-12}\,\mathrm{rad\,s^{-1}}$ for a drift time of about 3 s. Repeating this measurement every 3 s, each ASU will reach after one orbit of 90 min the level of $7 \cdot 10^{-14}\,\mathrm{rad\,s^{-1}}$, in the course of 1 year the level of $2 \cdot 10^{-15}\,\mathrm{rad\,s^{-1}}$, i.e. a tenth of the expected effect.

5 Coherent Atom Sensors: BEC and Atom Lasers

Dense *ultra-cold* samples of atoms are now routinely produced in laboratories all around the world. Using evaporative cooling techniques [19–21], one can cool a cloud of a few 10^6 atoms to temperatures below 100 nK [87]. At a sufficiently low temperature and high density, a cloud of atoms undergoes a phase transition to quantum degeneracy. For a cloud of bosonic (integer spin) atoms, this is known as *Bose–Einstein condensation*, in which all the atoms accumulate in the same quantum state (the atom-optical analog of the laser effect in optics). A BEC exhibits long-range correlation [24, 25, 88] and can therefore be described as a coherent "matter wave": an ideal candidate for the future of atom interferometry in space. The extremely low temperature associated with a BEC results in a very slow ballistic expansion, which in turn leads to interrogation times of the order of several tens of seconds in a space-based atom interferometer. In addition, the use of such a coherent source for atom optics could give rise to novel types of atom interferometry [28, 29, 52, 62, 89, 90].

5.1 Atom Laser: A Coherent Source for Future Space Applications

The idea for an atom laser pre-dates the demonstration of the exotic quantum phenomenon of BEC in dilute atomic gases. But it was only after the first such condensate was produced in 1995 that the pursuit to create a laser-like source of atomic de Broglie waves became intense.

In a Bose–Einstein condensate all the atoms occupy the same quantum state and can be described by the same wave function. The condensate therefore has many unusual properties not found in other states of matter. In particular, a Bose condensate can be seen as a coherent source of matter waves. Indeed, in a (photonic) laser all the photons share the same wave function. This is possible because photons have an intrinsic angular momentum, or "spin", equal to the Planck's constant $\hbar$. Particles that have a spin that is an integer multiple of $\hbar$ obey Bose–Einstein statistics. This means that more boson can occupy the same quantum state. Particles with half-integer spin – such as electrons, neutrons and protons, which all have spin $\hbar/2$ – obey Fermi–Dirac statistics. Only one fermion can occupy a given quantum state.

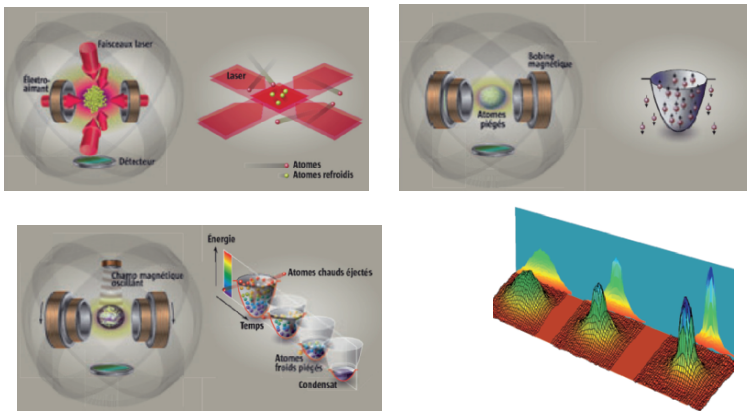

Fig. 15. Evaporative cooling towards Bose–Einstein condensation (from [91]). Initially, atoms are trapped in optical molasses using radiative forces. Then, the atoms are transferred in magnetic trap where they can stay trapped for hundred of seconds. Since no damping exists in such trap (as opposed to radiative traps), an evaporative cooling technique is used to remove the hottest atoms. In this technique, the trap is capped at a chosen height (using RF-induced spin flip) and the atoms with higher energy escape. By lowering the trap height, an ultra-cold high-density sample of atoms is obtained. The *bottom right picture* shows the BEC transition where a tiny dense peak of atoms (a coherent matter wave) appears at the centre of a Maxwell–Boltzman distribution (incoherent background).

A composite particle, such as an atom, is a boson if the sum of its protons, neutrons and electrons is an even number; the composite particle is a fermion if this sum is an odd number. Rubidium-87 or Caesium-133 atoms, for example, are bosons, so a large number of them can be forced to occupy the same quantum state and therefore have the same wave function. To achieve this, a large number of atoms must be confined within a tiny trap and cooled to sub-millikelvin temperatures using a combination of optical and magnetic techniques (see for example [92]). The Bose–Einstein condensates are produced in confining potentials such as magnetic or optical traps by exploiting either the atom's magnetic moment or an electric dipole moment induced by lasers (Fig. 15). In a magnetic trap, for instance, once the atoms have been cooled and trapped by lasers, the light is switched off and an inhomogeneous magnetic field provides a confining potential around the atoms. The trap is analogous to the optical cavity formed by the mirrors in a conventional laser. To make a laser we need to extract the coherent field from the optical cavity in a controlled way. This technique is known as "output coupling". In the case of a conventional laser the output coupler is a partially transmitting mirror. Output coupling for atoms can be achieved by transferring them from states that are confined to ones that are not, typically by changing an internal degree of freedom, such as the magnetic states of the atoms. The development of such atom laser is providing atom sources that are as different from ordinary

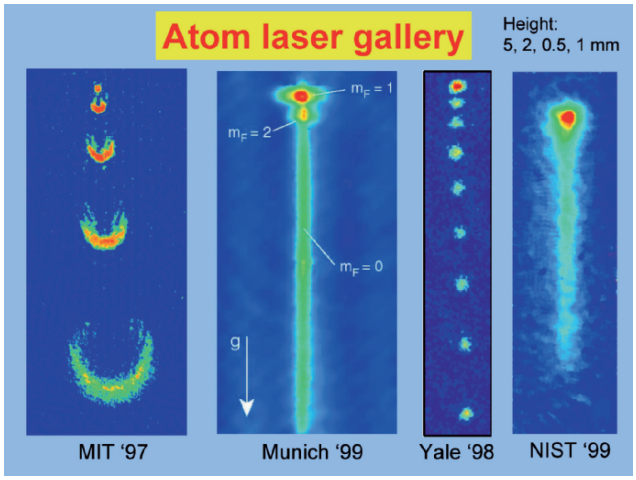

Fig. 16. Various types of atom lasers: (**a**) At MIT, intense RF pulses spin flips the atoms from a trapped state to an untrapped state. They fall under gravity. (**b**) In Yale, the condensate is loaded in an optical lattice. The combination of tunnel effect and gravity produces coherent pulses of atoms. (**c**) At NIST, Raman pulses extract atoms' pulses in a chosen direction. When the pulses overlap, a quasi-continuous atom laser is achieved. (**d**) In Munich, a weak RF coupler extracts a continuous atom wave from the condensate.

atomic beams as lasers are from classical light sources, and promises to outperform existing precision measurements in atom interferometry [28,29,90] or to study new transport properties [93–95].

The first demonstration of atomic output coupling from a Bose–Einstein condensate was performed with sodium atoms in a magnetic trap by W. Ketterle and co-workers at the Massachusetts Institute of Technology (MIT) in 1997. Only the atoms that had their magnetic moments pointing in the opposite direction to the magnetic field were trapped. The MIT researchers applied short radio-frequency pulses to "flip" the spins of some of the atoms and therefore release them from the trap (see Fig. 16a). The extracted atoms then accelerated away from the trap under the force of gravity. The output from this rudimentary atom laser was a series of pulses that expanded as they fell due to repulsive interactions between the ejected atoms and those inside the trap. Later T. Hänsch and colleagues at the Max Planck Institute for Quantum Optics in Munich extracted a continuous atom beam that lasted for 0.1 s. The Munich team used radio-frequency output coupling in an experimental setup that was similar to the one at MIT but used more stable magnetic fields (see Fig. 16b). Except for a few cases [24,96], the outcoupling methods do not allow to chose neither the direction nor the wavelength of the atom laser beam. In addition, the intrinsic repulsion between the atom laser beam and the BEC has dramatic effects [97,98] and gravity plays a significant role [99], such that the atom laser wavelength becomes rapidly small (Fig. 17).

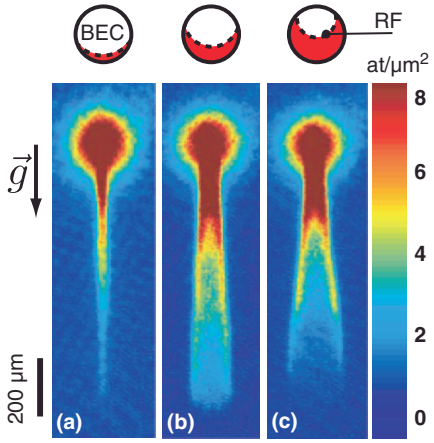

Fig. 17. Absorption images of a non-ideal atom laser, corresponding to density integration along the elongated axis x of the BEC. The figures correspond to different heights of RF-outcoupler detunings with respect to the bottom of the BEC: (**a**) $-0.37\,\mu$m, (**b**) $-2.22\,\mu$m, (**c**) $-3.55\,\mu$m. The *graph* above shows the RF-outcoupler (*dashed line*) and the BEC slice (*red*) which is crossed by the atom laser and results in the observation of caustics. The field of view is $350\times1{,}200\,\mu\text{m}^2$ for each image.

The solution to overcome these limitations is either to develop coherent sources in space [90] or to suspend the atom laser during its propagation. For the latter, many atomic waveguides have been developed for cold thermal beams [100–107] or even for degenerate gases [95,108,109]. Nevertheless, as in optics, the transfer of cold atoms from magneto-optical traps into these small atom guides represents a critical step and so far, coupling attempts using either cold atomic beams [102,110] or cold atomic clouds [101,104,105,111] have led to relatively low coupling efficiency. To increase this efficiency, a solution consists in creating the atom laser directly into the guide [112], leading eventually to a continuous guided atom laser [113] analogous to the photonic fibre laser. This has been recently achieved in Orsay (LCFIO), where the BEC from which the atom laser is extracted from is *pigtailed* to the atom guide. In this setup, an atom laser is outcoupled from a hybrid opto-magnetic trap to a optical guide. The propagation direction is fixed by the propagation direction of the dipole trap laser beam and the velocity of the outcoupled atoms can be controlled by carefully adjusting the guide parameters. Using this scheme, atomic de Broglie wavelengths as high as $0.7\,\mu$m was observed (Fig. 18).

5.2 Application to $\hbar/m$ Measurement

The quantized exchange of momentum between light and atoms has opened the way to measurements of the de Broglie–Compton frequency of atomic species mc^2/h by direct frequency measurements [141]. The use of cold atom

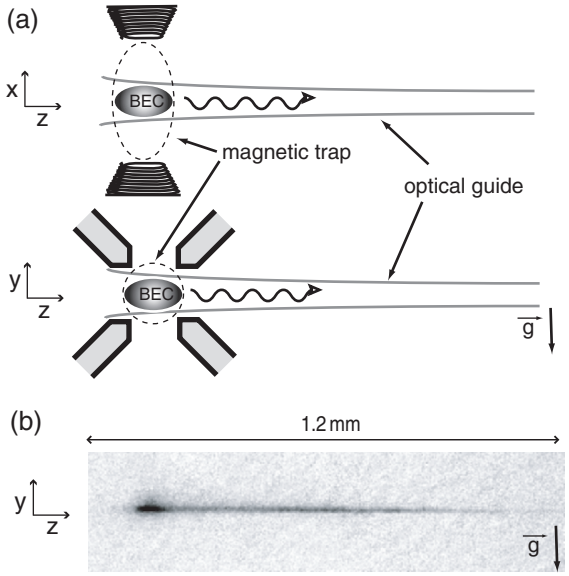

Fig. 18. (**a**) Schematic view of the setup. The BEC is obtained in a crossed hybrid magnetic and optical trap. The optical trap is horizontal. Its focus is shifted in the longitudinal direction z so as to attract the atoms. (**b**) Experimental absorption image of a guided atom laser after 50 ms of outcoupling. The imaging is along the x-axis.

interferometric techniques has subsequently led to very accurate determinations of the fine structure constant α from the ratio of the Rydberg constant to this frequency [18, 60].

Among the various new experiments aiming to improve these measurements of α via the measurement of the ratio $\hbar/m$, two experiments demonstrated a coherent matter-wave interferometer based on Bragg scattering [29, 90]. In the following, we shall review the measurement achieved in the Groupe d'Optique Atomique in Orsay (LCFIO).

Principle of Bragg Scattering

The principle of Bragg scattering is the following [114, 115]: two counter-propagating laser beams of wave vector $\pm\boldsymbol{k}_\mathrm{L}$ and frequencies ν_L and $\nu_\mathrm{L} + \delta\nu$ form a moving light grating. The common frequency ν_L is chosen to be in the optics domain but far detuned from atomic resonances to avoid spontaneous emission. A two-photon transition, involving absorption of a photon from one beam and stimulated re-emission into the other beam, results in a coherent transfer of momentum $\boldsymbol{p}_\mathrm{f} - \boldsymbol{p}_\mathrm{i} = 2\hbar\boldsymbol{k}_\mathrm{L}$ from the light field to the atoms, where $\boldsymbol{p}_\mathrm{i}$ and $\boldsymbol{p}_\mathrm{f}$ are the initial and final momenta of the atoms. Conservation of energy and momentum leads to the resonance conditions $E_\mathrm{f} = E_\mathrm{i} + h\delta\nu$,

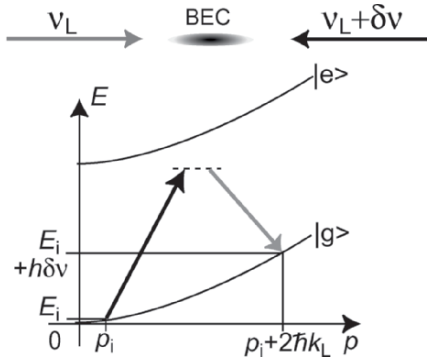

Fig. 19. Principle of Bragg scattering: a moving standing wave, formed from two counter-propagating laser beams with a small relative detuning $\delta\nu$, can coherently transfer a fraction of the atoms to a state of higher momentum when the resonance condition is fulfilled. A two-photon Bragg scattering event imparts a momentum $2\hbar k_{\mathrm{L}}$, and an energy of $h\delta\nu$ to the atoms: thus, the first-order (two photon) Bragg resonance for atoms with zero initial velocity occurs at a detuning of $h\delta\nu = 4\hbar^2 k_{\mathrm{L}}^2/2m$. This resonance condition depends on the initial velocity of the atoms relative to the optical standing wave.

where (in free space) the initial and final energies of the atoms are given by $E_{\mathrm{i}} = p_{\mathrm{i}}^2/2m$ and $E_{\mathrm{f}} = p_{\mathrm{f}}^2/2m$, respectively. Bragg scattering can be used for different types of matter-wave manipulation, depending on the pulse length τ. Using a short pulse ($\tau < 100\,\mu$s), the Bragg beams are sufficiently frequency broadened that the Bragg process is insensitive to the momentum distribution within the condensate: the resonance condition is then satisfied simultaneously for the entire condensate. If the Bragg laser power and pulse duration are then selected to correspond to the $\pi/2$ condition, the probability of momentum transfer to the atoms is 50%: this is a 50/50 beam splitter for the condensate, between two different momentum states. When using longer pulses (for example $\tau = 2$ ms in [116]), the Bragg process is velocity selective, and one can apply this technique to momentum spectroscopy [88, 116] (Fig. 19).

$\hbar/m$ Measurement

The experimental sequence proceeds as follows [116,117]: a laser-cooled sample of ^{87}Rb atoms is magnetically trapped in the $5\mathrm{S}^{1/2}|F = 1, m_F = -1\rangle$ state and then evaporatively cooled to quantum degeneracy. The magnetic trapping fields are switched off and the atoms fall for 25 ms. During this free-fall period, the coherent Bragg scattering "velocimeter" pulse is applied. In this experiment, the implementation of Bragg scattering is as follows: two orthogonally polarised, co-propagating laser beams of frequencies ν_L and $\nu_L + \delta\nu$ and wave vector $\boldsymbol{k}_{\mathrm{L}}$ are retroreflected by a highly stable mirror, with 90° polarisation rotation (see Fig. 20). With this scheme, the atoms are submitted

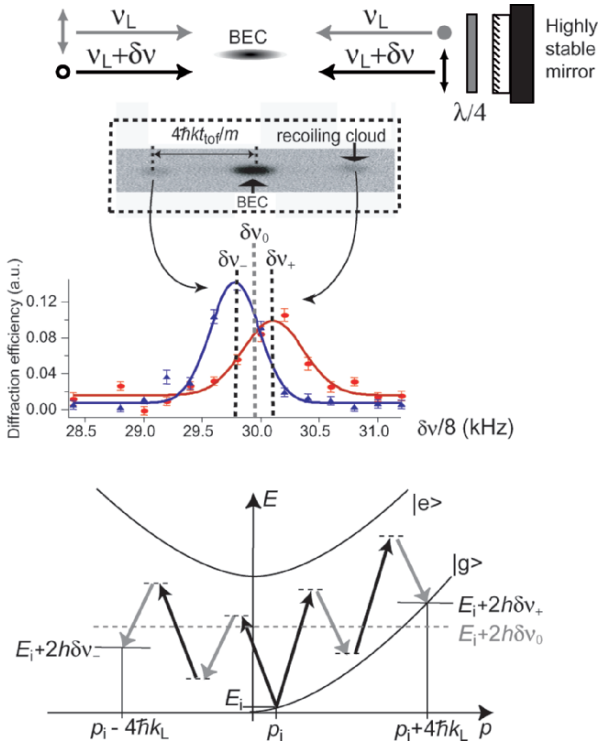

Fig. 20. Principle of our four photon, dual direction Bragg scattering scheme. *Top*: schematic of the experimental apparatus. Two retroreflected laser beams form two standing waves of orthogonal polarisations, moving in opposite directions. *Middle*: normalised number of atoms diffracted into each of the two output channels as a function of Bragg detuning $\delta\nu$. (*Inset*: typical absorption image after Bragg diffraction and free evolution during a time t_{tof}.) *Bottom*: schematic picture of the four-photon Bragg resonance condition. For zero initial momentum, the resonance condition is fulfilled by both standing waves for a detuning $\delta\nu_0$. For non-zero initial momentum p_{i}, the resonance frequency is equally and oppositely shifted for each of the two channels.

to two standing waves moving in opposite directions and with orthogonal polarisations. In addition, the relative detuning $\delta\nu$ is chosen so as to fulfill the second-order (four photon) resonance condition. This four laser Bragg scattering scheme produces a coherent transfer of momentum of $+4\hbar\boldsymbol{k}_{\mathrm{L}}$ and $-4\hbar\boldsymbol{k}_{\mathrm{L}}$. This scheme enables to reject the effect of a non-zero initial velocity, which can arise from imperfections in the magnetic trap switch-off. For an initial velocity p_{i}/m, the four-photon resonance conditions for the two oppositely moving standing waves are $\delta\nu_+ = \delta\nu_0(1+p_{\mathrm{i}}/2\hbar k_{\mathrm{L}})$ and $\delta\nu_- = \delta\nu_0(1-p_{\mathrm{i}}/2\hbar k_{\mathrm{L}})$, where $\delta\nu_0$ is the Doppler-free value, $\delta\nu_0 = (8/2\pi)(\hbar k_{\mathrm{L}}^2/2m)$ (see Fig. 20). Scanning the Bragg scattering efficiency in the two directions as a function of $\delta\nu$ yields two peaks with widths corresponding to the condensate momentum width,

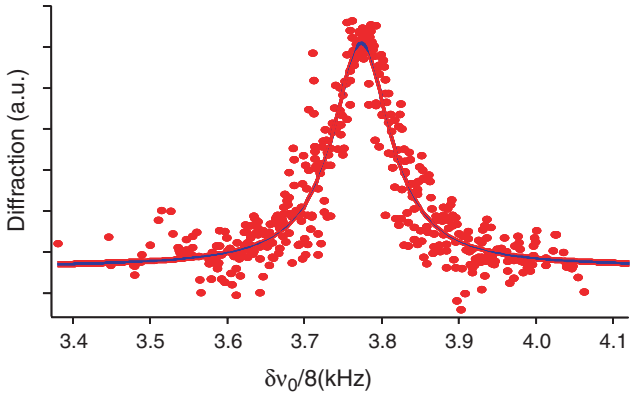

Fig. 21. Final spectrum (corrected for Doppler effect). The fit to this spectrum yields the centre frequency $\delta\nu_0$, from which we obtain the ratio h/m.

centred at each of the resonance frequencies, $\delta\nu_+$ and $\delta\nu_-$ (Fig. 20). After fitting each individual spectrum with a Gaussian distribution, the two centre frequencies $\delta\nu_\pm$ are extracted. To correct the data for the non-zero initial velocity, both spectra are then centred around the average value $\delta\nu_0 = (\delta\nu_+ + \delta\nu_-)/2$.

After averaging over 350 spectra (Fig. 21), the centre detuning was measured to be $\delta\nu_0 = 30.189(4)\,\mathrm{kHz}$ where the figure in parentheses is the 68% confidence interval of the fit. This corresponds to a value $h/m \equiv \lambda^2 \times \delta\nu_0/4 = 4.5946(7)\cdot 10^{-9}\,\mathrm{m^2\,s^{-1}}$ where the wavelength $\lambda = 780.246291(2)\cdot 10^{-9}$ of the Bragg beams, slightly detuned from the $\left(5^2\mathrm{S}_{1/2}, \mathrm{F}=2\right) \rightarrow \left(5^2\mathrm{P}_{3/2}, \mathrm{F}=3\right)$ optical transition, is very accurately known from [118,119]. The offset between the measurement and the CODATA value of h/m ($4.59136\cdot 10^{-9}\,\mathrm{m^2\,s^{-1}}$) can be explained by two major systematic effects. First, as described in [116], the frequencies ν_L and $\nu_L + \delta\nu$ of the Bragg scattering beams were obtained by using two independently driven acousto-optical modulators (AOM) of centre frequency 80 MHz. The frequency difference $\delta\nu$ was then deduced from the measurement of the frequency of each AOM driver with a high-precision frequency metre that had an accuracy of about 4×10^{-7}, giving a $\pm 16\,\mathrm{Hz}$ inaccuracy in the actual frequency difference $\delta\nu$. The resulting systematic error then gives $h/m = 4.5946(20)(7)\cdot 10^{-9}\,\mathrm{m^2\,s^{-1}}$. The second systematic effect is a collisional shift due to interactions in the high-density atomic cloud.

Effects of Interactions in a High-Density Atomic Sample

Ultra-cold ^{87}Rb atoms have repulsive interactions which modify the Bragg scattering resonance condition. The energy of an atom in the condensate is $E_\mathrm{i} = p_\mathrm{i}^2/2m + Un(\mathbf{r})$. The second term is the condensate interaction energy: $n(\boldsymbol{r})$ is the local atomic density of the condensate and $U = 5.147(5)\times 10^{-51}\,\mathrm{J\,m^3}$ is the interaction parameter. Immediately after Bragg scattering

into a different momentum state, an atom experiences an effective potential $2Un(\boldsymbol{r})$ due to the surrounding condensate, and its energy is then $E_\mathrm{f} = p_\mathrm{f}^2/2m + 2Un(\boldsymbol{r})$ [88]. We can therefore replace the Bragg resonance condition (for zero initial momentum) with a *local* resonance condition which takes into account the effect of interactions:

$$2h\delta\nu_0(\boldsymbol{r}) = 16\frac{\hbar^2 k_\mathrm{L}^2}{2m} + Un(\boldsymbol{r}) \tag{8}$$

The parabolic density distribution of our Bose–Einstein condensate, at the time where the Bragg diffraction occurs, is

$$n(x,y,z) = n_0 \cdot \max\left[0\,;\, 1-(x^2+y^2)/R_\perp^2 - z^2/R_z^2\right]$$

with peak density $n_0 \simeq 3.6(4)\cdot 10^{18}\,\mathrm{m}^{-3}$ and half-lengths $R_\perp \simeq 9.8\,\mu\mathrm{m}$ and $R_z \simeq 126\,\mu\mathrm{m}$, where z is the direction of the Bragg scattering. Since the above measurement of the diffraction efficiency averages over the whole cloud, the resulting spectrum is then shifted by $U\langle n\rangle/2h \sim 4Un_0/7$ and broadened. Taking this interaction shift into account, the corrected measured value of h/m is:

$$\frac{h}{m} = \frac{\lambda^2}{4}\left(\langle\delta\nu_0\rangle - \frac{U\langle n\rangle}{2h}\right) \simeq 4.5939(21)(7)\cdot 10^{-9}\,\mathrm{m}^2\,\mathrm{s}^{-1}, \tag{9}$$

which is in agreement with the CODATA value.

5.3 The Prospect and Limits of High-Density Coherent Samples

The fact that ultra-cold bosons interact is a major drawback for precision measurements using atom interferometry. In the above experiment, interactions result in a systematic shift as well as a decrease in measurement precision. In principle, the systematic shifts can be calculated. However, the interaction parameter U is hard to measure and is generally not known to better than $\sim 10^{-4}$. The atomic density is also subject to time fluctuations and is difficult to know to better than $\sim 10^{-2}$, reducing the absolute accuracy. In addition, as shown in earlier experiments [116, 120], interactions produce a loss of coherence of the atomic samples at ultra-low, finite temperatures, limiting the maximum interrogation time of a coherent matter-wave atom interferometer. Finally, even at zero temperature, the mean-field energy due to interactions is converted into kinetic energy during free fall, giving rise to a faster ballistic expansion. This last effect will ultimately reduce interrogation times.

The Need of an Ideal Coherent Atomic Source

From the observations of both MIT and Orsay, we conclude that one should ideally use an interaction-free, ultra-cold atomic source for ultimate-precision atom interferometry in space. Using bosons, one could think of two ways of

decreasing interaction effects. Close to a Feshbach resonance [121], one can control the interaction parameter U, which can be made equal to zero for a certain magnetic field [122, 123]. However, magnetic fields introduce further systematic shifts that are not controllable to within a reasonable accuracy. Alternatively, one could try to decrease the density of the sample of atoms, but the production of large atom number, ultra-low density Bose–Einstein condensate is a technical challenge not yet overcome [124].

A promising alternative solution is to use quantum-degenerate fermionic atomic sources [61]. The Pauli exclusion principle forbids symmetric two-body collision wave functions, so at zero temperature a sample of neutral atomic fermions has no interactions. An ultra-cold fermionic source may still allow very long interrogation times, even if limited by the excess energy of the Fermi pressure, and would therefore be an ideal candidate for atom interferometry in space with ultimate precision and accuracy.

6 Research and Technology: Towards a Space Atom Sensor

Intense research effort has focused on the study of atom interferometers miniaturization since their first demonstration in 1990. Atom interferometers benefit from the use of trapped ultra-cold atomic gases, gaining good signal-to-noise ratios due to the high atomic densities, and the coherence required for the visibility of interference patterns due to the low temperatures [8]. Since the recent development of atom chip-based coherent sources, efforts to incorporate interferometry on an "atom chip" [125–128] are motivated by the large physical size of a traditional apparatus and a desire to better tailor interferometer geometries. Most attempts to implement a coherent beam splitter/recombiner on a chip have used current-induced magnetic fields, typically forming double potential wells that merge and then split apart either in space, in time, or in both. Nevertheless, except in one experiment [129], various technical issues, such as noise coupled into the current and roughness or impurities of the wires, have stymied attempts to demonstrate on-chip interference. On the other hand, *traditional* light-pulse interferometer demonstrated already very high performances. Thus, efforts to reduce the size such as the CASI, GOM and Girafon scientific programs might lead to future small size, industrial atom interferometry inertial sensors. In fact, such transportable sensors are already available in the group of M. Kasevich at Stanford (Fig. 22).

The sensitivity of an interferometric measurement also depends on the interrogation time, the time during which the sample freely evolves. This time is limited by both the free fall of the atomic cloud, requiring tall vacuum chambers, and by its free expansion, demanding extra-sensitive detection systems for extremely dilute clouds. Ultra-low temperatures further reduce the expansion and should allow for more compact systems and for the full use of the

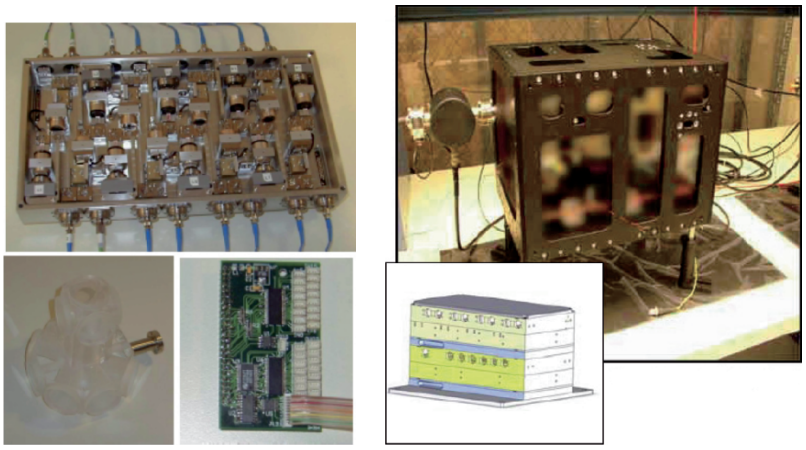

Fig. 22. The transportable interferometers developed at Stanford in M. Kasevich group (credit M. Kasevich).

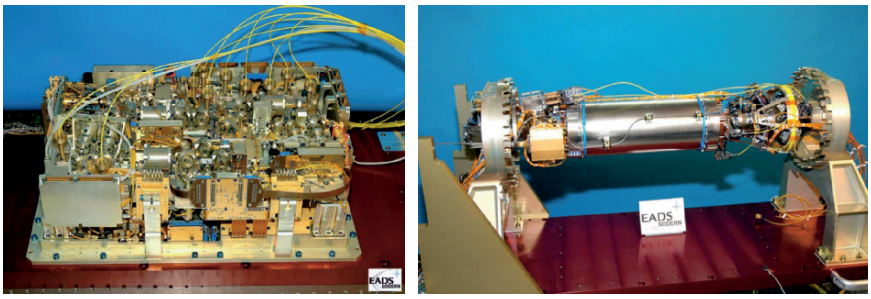

Fig. 23. The space clock PHARAO (courtesy EADS SODERN). *Left*: Photograph of the integrated laser source with cover removed. The dimensions are $530 \times 350 \times 150\,\mathrm{mm}^3$ and the mass is 20.054 kg. The ten polarisation-maintaining optical fibres in *yellow* guide the laser beams to the caesium tube. All diode lasers (JDSU) are mounted on a Peltier cooler for temperature regulation within 2 mK. *Right*: The integrated caesium tube without the two external magnetic shields. The volume is $990 \times 336 \times 444\,\mathrm{mm}^3$ and the total mass is 44 kg.

long free-fall time offered by a micro-gravity environment. For that purpose, the French space agency CNES is funding and acting as the prime contractor of the PHARAO clock, a micro-gravity atomic clock which was designed by SYRTE, LKB and CNES building upon several years of experience with cold atom fountain frequency standards using caesium and rubidium atoms. After the first free-fall demonstration in a zero-g Airbus, the clock industrial development began in 2002 by the realisation of an engineering model representative of the flight model in terms of interfaces, design and fully functional (Fig. 23).

As far as atom interferometry is concerned, the fact that bosons suffer from interaction shifts leading to systematic errors might prevent to achieve the ultimate limit of those sensors. As for the clock case, this problem might not be apparent in ultra-cold fermions [130]. However, degenerate fermions have an intrinsically broad momentum distribution due to Pauli blocking, limiting the visibility of interference patterns. Furthermore, to achieve quantum degeneracy, fermions must be cooled using a buffer gas, typically an ultra-cold gas of bosons, thus complicating experiments using fermions. Pairs of fermions (molecules or Cooper pairs [131]) can be created by applying a homogeneous magnetic field (Feshbach resonances [132]), offering yet more possible candidate species for atom interferometers.

A further bonus to free fall is the possibility of using weaker confining forces for the atoms, since gravity need not be compensated with additional levitation forces [124]. Temperatures achieved by evaporative cooling and adiabatic expansion are lowered as the trapping potential is reduced. Not only does the sensitivity of an interferometric measurement benefit, but also new phases of matter may be observed if the kinetic energy can be made smaller than the interatomic potential. A reduced-gravity environment will permit study of new physical phenomena, e.g. spin dynamics and magnetic ordering (see for example [133] and references therein).

6.1 ICE: Towards a Coherent Atom Sensor for Space Applications

The objective of ICE [134], a CNES-funded project that share the experience of various partners (SYRTE, ONERA and IOTA), is to produce an accelerometer for space with a coherent atomic source. It uses a mixture of Bose–Einstein condensates with two species of atoms (Rb and K) to carry out a first comparison of accelerations measured by the two different types of atomic species (with two bosons and one boson and one fermion). The central components of this project are the atomic physics vacuum system, the optics and their supports. The atomic manipulation starts with alkali-metal vapour dispensers for rubidium and potassium [135]. A slow jet of atoms is sent from the collection chamber by a dual species, 2D-MOT to the trapping chamber, for collection and cooling in a 3D-MOT. Atoms are then to be transferred to a conservative, far-off-resonance optical-dipole trap (FORT) for further cooling towards degeneracy. The sample is then ready for coherent manipulation in an atom interferometer. Raman two-photon transition will be used as atomic beam splitters and mirrors. Three-pulse sequences ($\pi/2 - \pi - \pi/2$) will be used for accelerometry.

As for the Girafon project, all light for the experiment arrives by optical fibres, making the laser sources independent of the vacuum system. Transportable fibred laser sources for laser cooling and trapping have been fabricated with the required frequency stability. The techniques for mechanically stable power distribution by free-space fibre couplers function according to specifications. The vacuum chamber is compatible with the constraints of

micro-gravity in an Airbus parabolic flight. Such a flight permits total interrogation times up to 7 s, giving a potential sensitivity of better than $10^{-9}\,\mathrm{m\,s^{-2}}$ per shot, limited by phase noise on the frequency reference for the Raman transitions.

6.2 Laser Systems

Continuous-Wave Fibre-Laser Source at 780 nm for Rubidium Cooling

An entirely pigtailed laser source is particularly appropriate in our case as it does not suffer from misalignments due to environmental vibrations. Moreover, telecommunication laser sources in the C-band (1,530–1,570 nm) have narrow linewidths ranging from less than 1 MHz for laser diodes, down to a few kHz for Erbium-doped fibre lasers. By second-harmonic generation (SHG) in a non-linear crystal, these 1.56 µm sources can be converted to 780 nm sources [136–138]. Such devices avoid the use of extended cavities as their linewidths are sufficiently narrow to satisfy the requirements of laser cooling.

The laser setup is sketched in Fig. 24. A 1,560 nm Erbium-doped fibre laser is amplified by a 500 mW polarisation-maintaining (PM) Erbium-doped fibre amplifier (EDFA). A 90/10 PM fibre coupler directs 10% of the pump power to a pigtailed output. Ninety per cent of light is then sent into a periodically poled Lithium–Niobate waveguide (PPLN-WG). This crystal is pigtailed on both sides with 1,560 nm single-mode fibres. The input fibre is installed in a polarisation loop system to align the electric field with principal axes of the crystal. A fibre coupler, which is monomode at 780 nm, filters pump light after the crystal and sends half of the 780 nm light into a saturated-absorption spectroscopy device for frequency servo-control. The other half is the frequency-stabilised pigtailed output. The whole device, including the frequency control electronics, was implemented in a rack for ease of transport. Typical output from the first generation device was 500 µW of 780 nm light, with more than 86 dB attenuation of 1,560 nm light after 3 m of monomode fibre. A more recent version (> 50 mW) has been used to power a MOT.

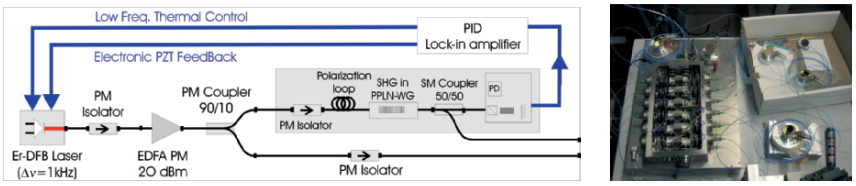

Fig. 24. *Left*: Transportable laser setup schematic. A double-loop feedback system is used for frequency control: the first returns a saturated absorption signal to the piezoelectric transducer; the second loop compensates thermal drifts of the fibre laser when the error signal of the first loop becomes large. *Right*: The fibre splitters developed at SYRTE.

Fibre Power Splitters

The optical bench and the vacuum chamber are not rigidly connected to each other, and laser light is transported to the vacuum chamber using optical fibres. Stability in trapping and coherent atom manipulation is assured by using only polarisation-maintaining fibres. Six trapping and cooling laser beams are needed for the 3D-MOT and five for the 2D-MOT, with relative power stability better than a few per cent. The fibre beam splitters are based on polarising cubes and half-wave plates with one input fibre and the relevant number of output fibres. The stability of the beam splitters has been tested by measuring the ratio of output powers between different outputs as a function of time. Fluctuations are negligible on short timescales (less than 10^{-4} relative intensity over 1 s), and very small over typical periods of experimental operation (less than 1% over a day). Even over months, drifts in power distribution are only a few per cent, which is sufficient for this experiment.

6.3 Mechanical and Vacuum Systems

The mechanical construction of the apparatus is critical to any free-fall experiment. Atomic physics experiments require heavy vacuum systems and carefully aligned optics. The ICE design is based around a cuboidal frame of foam-damped hollow bars with one face being a vibration-damped optical breadboard (see Fig. 25). The outside dimensions are $1.2 \times 0.9 \times 0.9\,\mathrm{m}^3$, and the total weight of the final system is estimated to be 400 kg (excluding power supplies, lasers, control electronics, air and water flow). The frame provides support for the vacuum system and optics, which are positioned independently of one another. The heavy parts of the vacuum system are rigged to the frame using steel chains and high-performance polymer slings under

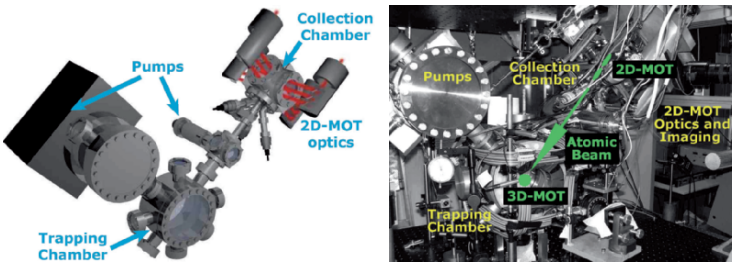

Fig. 25. *Left*: Artist's impression of the vacuum system. Atoms are transferred from the collection chamber, using a 2D-MOT, to the trapping chamber, where they are collected in a 3D-MOT. The trapping chamber has large optical accesses for the 3D-MOT, optical-dipole trap (FORT), imaging and interferometry. There is a getter pump between the two chambers to ensure a large pressure difference. The other pump is a combined ion pump–titanium sublimation pump. *Right*: The ICE mechanical structure with optics and light paths represented.

tension, adjusted using turnbuckles; most of the equipment being standard in re-creational sailing or climbing. The hollow bars have precisely positioned grooves which permit optical elements to be rigidly fixed (bolted and glued) almost anywhere in the volume within the frame. An adaptation for transportability will be to enclose the frame in a box, including acoustic and magnetic shielding, temperature control, air overpressure (dust exclusion), as well as ensuring safety in the presence of the high-power lasers.

The vacuum chamber has three main parts: the collection chamber (for the 2D-MOT), the trapping chamber (for the 3D-MOT and the FORT) and the pumps (combined ion pump and titanium sublimation pump). Between the collection and trapping chambers, there is an orifice and a getter pump, allowing for a high differential pressure, permitting rapid collection by the 2D-MOT but low trap losses in the 3D-MOT and FORT. The magnetic coils for the 2D-MOT are under vacuum, and consume just 5 W of electrical power.

To avoid heating due to vibrations in the FORT optics, or measurement uncertainties due to vibrations of the imaging system, the trapping chamber is as close as possible to the breadboard. For laboratory tests, the breadboard is at the bottom and the 2D-MOT arrives at 45° to the vertical, leaving the vertical axis available for addition of interferometry for precise measurements, e.g. a standing light wave. Around the main chamber, large electromagnet coils in Helmholtz configuration will be added to produce homogeneous stable fields up to 0.12 T (1,200 G), or gradients up to $0.6\,\mathrm{T\,m^{-1}}$ ($60\,\mathrm{G\,cm^{-1}}$).

2D MOT

The 2D-MOT is becoming a common source of cold atoms in two-chamber atomic physics experiments [66], and is particularly efficient for mixtures [139] of ^{40}K and ^{87}Rb, if isotopically enriched dispensers are used. Briefly, a 2D-MOT has four sets of beams (two mutually orthogonal, counter-propagating pairs) transversely to the axis of the output jet of atoms, and a cylindrical-quadrupole magnetic field generated by elongated electromagnet pairs (one pair, or two orthogonal pairs). Atoms are cooled transverse to the axis, as well as collimated. Implicitly, only slow atoms spend enough time in the 2D-MOT to be collimated, so the output jet is longitudinally slow. The number of atoms in the jet can be increased by the addition of the push beam, running parallel to the jet: a 2D-MOT$^+$. Typically the output jet has a mean velocity below $30\,\mathrm{m\,s^{-1}}$, with up to 10^{10} atoms per second of ^{87}Rb and 10^8 atoms per second of ^{40}K.

The ICE design uses 40 mW per species for each of the four transverse beams, each divided into two zones of about 20 mm using non-polarising beam-splitter cubes, corresponding to about three times the saturation intensity for the trapping transitions. The pushing beam uses 10 mW of power, and is about 6 mm in diameter. Each beam comes from an individual polarisation-maintaining optical fibre, with the light at 766.5 and 780 nm being superimposed on entry to the fibres. The 2D-MOT is seen as two bright lines of fluorescence in the collection chamber.

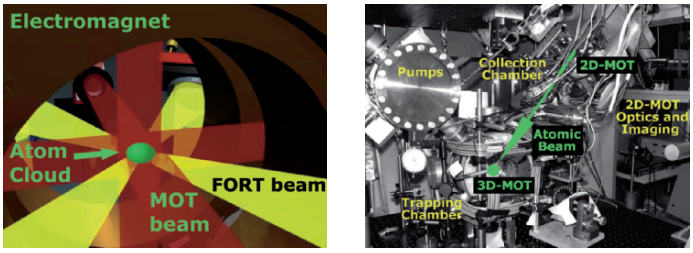

Fig. 26. *Left*: Artist's impression of the 3D-MOT (*dark, red beams*, and the electromagnets) and far-off-resonance optical-dipole trap (FORT; *pale, yellow beams*). *Right*: Photograph of the vacuum chamber, the support structure and the optics for magneto-optical traps. The main chamber has two very large viewports as well as seven side windows (and one entry for the atoms from the 2D-MOT). Thus there is plenty of optical access for the 3D-MOT, the FORT, imaging and interferometry. To preserve this optical access, the magnetic coils are outside of the chamber, although this markedly increases their weight and power consumption.

3D-MOT and Optical-Dipole Trap (Fig. 26)

The atomic jet from the 2D-MOT is captured by the 3D-MOT in the trapping chamber. At the time of writing, we have observed the transfer and capture of atoms, significantly increased by the addition of the pushing beam. The 3D-MOT uses one polarisation-maintaining fibre input per species. Beams are superimposed and split into six arms (on a small optical breadboard fixed near one face of the frame) for the three, orthogonal, counter-propagating beam pairs. Once enough number of atoms are collected in the 3D-MOT, the 2D-MOT is to be turned off, and the 3D-MOT optimised for transfer to the FORT.

The FORT consists of two nearly orthogonal (70°) beams making a crossed dipole trap using 50 W of light at 1,565 nm. Rapid control over intensity is achieved using an electro-optical modulator, and beam size using a mechanical zoom, after the design of Kinoshita et al. [140]. Optimisation of transfer from the 3D-MOT to the FORT, and the subsequent evaporative cooling, can be enhanced with strong, homogeneous, magnetic fields that will be used to control inter-species interactions via Feshbach resonances [132], to expedite sympathetic cooling of ^{40}K by ^{87}Rb. With the expected loading of the 3D-MOT during less than 5 s, then cool to degeneracy in the optical-dipole trap in around 3–10 s, ICE will be able to prepare a sample for interferometry in less than the free-fall time of a parabolic flight (around 20 s).

7 Conclusion

Previous experiments measuring the gravitational acceleration of Earth and its gradient or rotations have been demonstrated to be very promising. Sensitivities better than $1\,\mathrm{nrad\,s^{-1}\,Hz^{-1/2}}$ for rotation measurements and

$2 \cdot 10^{-8} \times g\,\mathrm{Hz}^{-1/2}$ for a gravity measurement have already been obtained. The sensitivity of matter-wave interferometers for rotations and accelerations increases with the measurement time and can therefore be dramatically enhanced by reducing the atomic velocity. Moreover, the use of optical transitions to manipulate the atomic wave packets enables an intrinsic knowledge of the scaling factor of these inertial sensors, which is directly linked to the frequency of the transition. Therefore, combining cold atomic sources and Raman transition-based atomic interferometers results in highly sensitive and highly accurate inertial sensors.

Going to space will enhance the benefit of cold atoms by increasing the interaction time, and opens up entirely new possibilities for research in fundamental physics or for inertial navigation with unprecedented precision, and operation in space is thus strong motivation for many ongoing projects.

Several missions along this line have thus only recently been proposed by NASA as well as ESA. Therefore, quantum sensors may be used as long-term inertial references for astronomy, deep-space navigation, or in missions to precisely map and monitor Earth's gravitational field (such as GOCE, etc.). In fundamental physics these space-based cold atom sensors may be the key for ground-breaking experiments on fundamental issues, such as gravitational wave astronomy (LISA-II, etc.) or the quest for a universal theory reconciling quantum theory and gravity (e.g. tests of the equivalence principle).

Cold atom quantum sensors display an excellent sensitivity for the absolute measurement of gravity, gravity gradients, magnetic fields as well as the Earth rotation and, thus, are particularly suited for applications in Earth sciences, or more generally for future "Earth watch" facilities. The range of fascinating applications of gravity mapping extends from earthquake and volcanic eruptions prediction, earth tectonics, to the search for oil and mineral resources, to the measurement of the effect of climate changes such as variations of the ocean level. As all these topics have a large impact on society as whole, the impact of improvements generated by this new technology will be accordingly high (large "leverage factor"). On the practical side such improvements should come from alleviating the need of constantly re-calibrating gravimeters (more than 1,500 deployed) in prospecting for natural resources, as atomic quantum sensors are intrinsically free of drift – or from alleviating the need of gyroscopically stabilised inertial platforms (expensive, large and service intensive) for mounting air- or sea-borne gravity gradiometers (more than 100 complex systems deployed), as multi-axes atomic quantum sensors can be made sufficiently orientation independent.

In addition, since quantum sensors rely on well-defined quantum mechanical properties of the atomic internal structure and the precisely known interaction with light, they may be used in new definitions of base units – similarly to what has already been done for time and frequency standards (atomic clocks) or for the practical realisation of resistance (quantum Hall effect) and voltage (Josephson effect). Immediate applications would be in the re-definition

of the kilogram, the only base unit in the international system of units (SI) that is defined by a material artefact of suspected stability. A very promising approach to overcome this unsatisfactory state of affairs is the use of a so-called *watt balance*, in which mechanical and electrical powers are compared. If the electrical power is measured in terms of the two quantum effects, the Josephson and the quantum Hall effect, the unit of mass can be linked to the fundamental Planck constant h through its de Broglie–Compton frequency $M_{\mathfrak{K}}c^2/h$. For proper operation, such a watt balance requires a "gravity reference" at a performance level that is difficult to achieve with classical sensors, but should be well within the range of capability of an atomic quantum gravimeter. The other way to determine the de Broglie–Compton frequency $M_{\mathfrak{K}}c^2/h$ of the kilogram is through the product of the Avogadro number by the de Broglie–Compton frequency $m_{\mathrm{u}}c^2/h$ of the atomic mass unit determined by atom interferometry [141]. Unfortunately these two ways do not yet agree at the $1.3 \cdot 10^{-6}$ level and further progress is necessary. As mentioned before the determination of $m_{\mathrm{u}}c^2/h$ by atom interferometry leads to a new determination of the fine structure constant α and hence to an experimental validation of the formula $R_K = h/e^2 = Z_0/2\alpha$ which is supposed to give the Von Klitzing resistance R_K compared to the vacuum impedance Z_0 in the Thompson–Lampard experiment.

Finally, handling BEC or atom lasers on ground or in space will be a leap towards the practical construction of cold coherent sources that can be used in ultra-high-precision atomic matter-wave sensors. Indeed, the long interrogation time requires a very strong collimation of the atomic source. Combining this with the high flux required for a high sensitivity leads to the need of an atom laser (like in optics, an atom laser is characterised by its high brilliance). On Earth, the best outcoupling device uses gravity to extract atoms from the magnetic cavity (except for the recent guided atom laser). Novel techniques can be explored in space, such as Raman output coupling, to extract a CW atom laser beam into a controlled propagation direction. In addition, novel types of atom interferometers using coherent sources, such as a resonant atom cavity [62] or a three-dimensional atom sensor [52], might be applied with these new sources. Ultimately, the correlation properties of the particles within the atom laser field may have a serious impact on the performance of future atom interferometer-based sensors. Hence, just as in the optical case, the sensitivity will be quantum limited by the uncertainty principle for the phase and number quadratures for single-mode operation. It is possible to go beyond this standard quantum limit with a coherent source prepared in phase–number squeezed states, i.e. Heisenberg-limited interferometry. Alternatively, entangled two-mode operation schemes, like the correlated emission laser (CEL) in laser physics, can also be used to suppress quantum noise in the relative phase.

Acknowledgements

The authors would like to express their deep thanks to the numerous colleagues who have contributed to the figures and results reported in this review and to the funding actors of the field, especially CNES, DGA and IFRAF.

References

1. W.W. Chow, J. Gea-Banacloche, L.M. Pedrotti, V.E. Sanders, W. Schleich, and M.O. Scully, *Rev. Mod. Phys.*, **72**, 61 (1985).
2. J.F. Clauser, *Physica B*, **151**, 262 (1988).
3. R. Colella, A.W. Overhauser, and S.A. Werner, *Phys. Rev. Lett.* **34**, 1472 (1975).
4. S.A. Werner, J.-L. Staudenmann, and R. Colella, *Phys. Rev. Lett.*, **42**, 1103 (1979).
5. Ch.J. Bordé, Ch. Salomon, S. Avrillier, A. Van Lerberghe, Ch. Bréant, D. Bassi and G. Scoles, *Phys. Rev. A* , **30**, 1836 (1984) and references therein.
6. F. Riehle, Th. Kisters, A. Witte, J. Helmcke and Ch.J. Bordé, *Phys. Rev. Lett.* **67**, 177 (1991).
7. M. Kasevich and S. Chu, *Appl. Phys.*, **B 54**, 321 (1992).
8. P.R. Berman (ed.), *Atom Interferometry* (Academic Press, 1997).
9. T.L. Gustavson, P. Bouyer, M.A. Kasevich, *Phys. Rev. Lett.* **78**, 2046 (1997).
10. T.L. Gustavson, *et al. Class. Quantum Grav.* **17**, 1 (2000).
11. A. Peters, K.Y. Chung, B. Young, J. Hensley and S. Chu, *Phil. Trans. R. Soc. Lond.* **A 355**, 2223 (1997).
12. A. Peters, K. Y. Chung and S. Chu, *Metrologia*, **38**, 25 (2001).
13. M. Kasevich and S. Chu, *Phys. Rev. Lett.* **67**, 181 (1991).
14. D.W. Keith, C.R. Ekstrom, Q.A. Turchette, and D.E. Pritchard, *Phys. Rev. Lett.* **66**, 2693 (1991).
15. M.J. Snadden *et al., Phys. Rev. Lett.* **81**, 971 (1998).
16. Ch. J. Bordé. In P.G. Bergmann and V. de Sabbata (eds.). *Advances in the Interplay between Quantum and Gravity Physics* (Kluwer Academic Publisher, 2002) pp. 27–55.
17. M. Fattori *et al., Phys. Lett.* **A 318**, 184 (2003).
18. A. Wicht *et al.*, *Proceeding of the 6th Symposium on Frequency standards and metrology* (ed. Patrick Gill, World Scientific, 2001) 193, *Physica Scripta*, **102**, 82 (2002).
19. M.H. Anderson *et al.*, *Science* **269**, 198 (1995).
20. K.B. Davis *et al.*, *Phys. Rev. Lett.* **75**, 3969 (1995).
21. C.C. Bradley, C.A. Sackett, and R.G. Hulet, *Phys. Rev. Lett.* **75**, 1687 (1995).
22. M.-O. Mewes *et al., Phys. Rev. Lett.* **78**, 582 (1997).
23. B.P. Anderson and M.A. Kasevich, *Science* **282**, 1686 (1998).
24. E.W. Hagley *et al. Science* **283**, 1706 (1999).
25. I. Bloch, T.W. Hänsch, and T. Esslinger, *Phys. Rev. Lett.* **82**, 3008 (1999).
26. G. E. Stedman *et al., Phys. Rev.* **A 51**, 4944 (1995).
27. G.E. Stedman, *Rep. Prog. Phys.* **60**, 615 (1997).
28. P. Bouyer and M. Kasevich, *Phys. Rev.* **A 56**, R1083 (1997).

29. S. Gupta, K. Dieckmann, Z. Hadzibabic, and D.E. Pritchard, *Phys. Rev. Lett.* **89**, 140401 (2002).
30. Hyper-Precision Cold Atom Interferometry in Space (HYPER), Assessment Study Report ESA-SCI(2000)10, European Space Agency (2000).
31. Ch.J. Bordé, *Phys. Lett.* **A 140**, 10 (1989).
32. D.M. Giltner, R.W. McGowan, and S.A. Lee, *Phys. Rev. Lett.* **75**, 2638 (1995).
33. C. Cohen-Tannoudji, *Cours au Collège de France* (1992–1993).
34. Ch. Antoine and Ch. J. Bordé, *Phys. Lett.* **A 306**, 277 (2003); *J. Opt. B: Quantum Semiclass. Opt.* **5**, S199 (2003).
35. P. Storey and C. Cohen-Tannoudji, *J. Phys. II France* **4**, 1999 (1994).
36. M. Kasevich, E. Riis, S. Chu, and R. de Voe, *Phys. Rev. Lett.* **63**, 612 (1989).
37. A. Clairon, C. Salomon, S. Guelatti, and W. Phillips, *Europhys. Lett.* **16**, 165 (1991).
38. Y. Sortais, S. Bize, and M. Abgrall, *Physica Scripta* **2001**, 50 (2001).
39. Ch.J. Bordé, *Metrologia* **39**, 435–463 (2002).
40. A. Peters, K. Chung, and S. Chu, *Metrologia* **38**, 25 (2001).
41. J.M. McGuirk *et al., Phys. Rev.* **A 65**, 033608 (2002).
42. K.U. Schreiber, A. Velikoseltsev, T. Klügel, M. Rothacher, G.E. Stedman and D.L. Wiltshire, *J. Geophys. Res.* **109** (B6): B06405 (2004).
43. T. Niebauer, G. Sasagawa, J. Faller, R. Hilt and F. Klopping, *Metrologia*, **32**, 159–180 (1995).
44. M. Kasevich, D. S. Weiss, E. Riis, K. Moler, S. Kasapi, and S. Chu, *Phys. Rev. Lett.* **66**, 2297 (1991).
45. K. Moler, D.S. Weiss, M. Kasevich, and S. Chu, *Phys. Rev.* **A 45**, 342 (1992).
46. A. Miffre *et al.*, to appear in *App. Phys.* **B**.
47. E.M. Rasel, M.K. Oberthaler, H. Batelaan, J. Schmiedmayer, and A. Zeilinger, *Phys. Rev. Lett.* **75**, 2633 (1995).
48. Ch.J. Bordé, in M. Ducloy, E. Giacobino, G. Camy (eds.), *Laser spectroscopy X* (World scientific, Singapore 1992), p. 239.
49. J.M. McGuirk, M.J. Snadden, and M.A. Kasevich, *Phys. Rev. Lett.* **85**, 4498 (2000)
50. Ch.J. Bordé, in J. Dalibard, J.-M. Raimond and J. Zinn-Justin (eds.) *Fundamental Systems in Quantum Optics*, Les Houches Lectures, Session LIII, 1990 (Elsevier Science Publishers, 1991).
51. Ch.J. Bordé, *C.R. Acad. Sci. Paris*, Série IV, **2**, 509 (2001).
52. Ch.J. Bordé, *Gen. Rel. Grav.* **36**, 475 (2004).
53. K. Bongs, R. Launais and M. Kasevich, to appear in App. Phys. B (2006).
54. Ch.J. Bordé, J.-C. Houard, and A. Karasiewicz, in C. Lämmerzahl, C.W.F. Everitt and F.W. Hehl (eds.): *Gyros, Clocks and Interferometers: Testing Relativistic Gravity in Space* (Springer, Berlin 2001), p. 403.
55. Ch.J. Bordé, A. Karasievicz, and Ph. Tourrenc, *Int. J. Mod. Phys.* **D 3**, 157 (1994).
56. S.N. Gupta, *Proc. Phys. Soc.* **A 65**, 161 (1952); *Proc. Phys. Soc.* **A 65**, 608 (1952).
57. R.P. Feynman, F.B. Morinigo, and W.G. Wagner, *Feynman Lectures on Gravitation*, edited by B. Hatfield (Addison-Wesley, Reading, Mass. 1995).
58. B.M. Barker, S.N. Gupta, and R.D. Haracz, *Phys. Rev.* **149**, 1027 (1966), and references therein.
59. M. Sagnac, *Compt. Rend. Acad. Sci.*, **157**, 708 (1913).

60. P. Cladé *et al., Europhys. Lett.*, **71** (5), pp. 730–736 (2005).
61. G. Modugno *et al*, arXiv:physics/0411097.
62. F. Impens, P. Bouyer and C. Bordé, to appear in App. Phys. B (2006).
63. P. Cheinet *et al.,* to appear in App. Phys. B (2006).
64. `http://www.onera.fr/actualites/2006-02.php`
65. B.P. Kibble, *Atomic Masses and Fundamental Constants* **5 ed** J H Saunders and A H Wapstra (Plenum, New York) pp 541–51 (1976).
66. K. Dieckmann, R.J.C. Spreeuw, M. Weidemüller and J.T.M. Walraven. *Phys. Rev.* **A 58**, 3891 (1998).
67. P. Cheinet, B. Canuel, F. Pereira Dos Santos, A. Gauguet, F. Leduc, A. Landragin, submitted for publication to: IEEE Trans. on Instrum. Meas., physics/0510197.
68. B. Mashhoon and D. Theiss, *Phys. Rev.* **D 49**, 1542 (1982).
69. B. Mashhoon, H. Paik, C. Will, *Phys. Rev.* **D 39**, 2285 (1989).
70. N. Sneeuw, R. Rummel, and J. Müller, *Class. Quantum Grav.* **58**, A113 (1996).
71. N. You *et al.*, to appear in App. Phys. B (2006).
72. A. Bertoldi *et al.,* physics/0606126.
73. C. Jekeli, *Geophysics* **58**, 508 (1993).
74. M. Moody and H. Paik, *Phys. Rev. Lett.* **70**, 1195 (1993).
75. H. Cavendish, *Philos. Trans. R. Soc.* **88**, 467 (1798).
76. G.T. Gillies, *Rep. Prog. Phys.* **60**, 151 (1997).
77. P.J. Mohr, B.N. Taylor, R*ev. Mod. Phys.* **72**, 351 (2000). The values can also be found at `http://www.physics.nist.gov/cuu/Constants/index.html`.
78. J.H. Gundlach, S.M. Merkowitz, *Phys. Rev. Lett.* **85** (2000) 2869; T.J. Quinn, C.C. Speake, S.J. Richman, R.S. Davis, A. Picard, *Phys. Rev. Lett.* **87** (2001) 111101.
79. J. Luo and Z.-K. Hu, *Class. Quantum Grav.* **17**, 2351 (2000).
80. J.P. Schwarz, D.S. Robertson, T.M. Niebauer, J.E. Faller, *Science* **282**, 2230 (1998).
81. B. Canuel *et al.*, *Phys. Rev. Lett.* **97**, 010402 (2006).
82. T. Gustavson, PhD. Thesis, Stanford University (2000).
83. G. Santarelli, Ph. Laurent, P. Lemonde, A. Clairon, A.G. Mann, S. Chang, A.N. Luiten, and C. Salomon, *Phys. Rev. Lett.* **82**, 4619 (1999).
84. D. Wineland *et al., Phys. Rev.* **A 46**, 6797 (1992).
85. H. Marion, F. Pereira Dos Santos, M. Abgrall, S. Zhang, Y. Sortais, S. Bize, I. Maksimovic, D. Calonico, J. Grünert, C. Mandache, P. Lemonde, G. Santarelli, Ph. Laurent, A. Clairon, and C. Salomon, *Phys. Rev. Lett.*, **90**, 150801 (2003).
86. H.J. Metcalf and P. Van Der Straten, *Laser Cooling and Trapping* (Springer Verlag, Berlin 1999).
87. W. Ketterle, Scientific American.com, Ask the Experts, January 19, 2004. Scientific American, May 2004, p. 120.
88. J. Stenger *et al., Phys. Rev. Lett.* **82**, 4569 (1999).
89. Y. Shin, M. Saba, T. Pasquini, W. Ketterle, D.E. Pritchard, and A.E. Leanhardt, *Phys. Rev. Lett.* **92**, 050405 (2004).
90. Y. Le Coq *et al.,* to appear in App. Phys. B (2006).
91. C. Westbrook, P. Bouyer, and C. Michaut, *La recherche* **67**, 40 (2003).
92. *When atoms behave as waves: Bose-Einstein condensation and the atom laser.* in: Les Prix Nobel 2001 (The Nobel Foundation, Stockholm, 2002), pp. 118–154. reprinted in: *ChemPhysChem* **3**, 736–753 (2002); *Rev. Mod. Phys.*, **74**, 1131–1151 (2002).

93. W. Hänsel, J. Reichel, P. Hommelhoff, and T.W. Hänsch, *Phys. Rev. Lett.* **86**, 608 (2001).
94. T. Paul *et al., Phys. Rev. A* **72**, 063621 (2005).
95. D. Clément *et al.*, *Phys. Rev. Lett.* **95**, 170409 (2005).
96. N.P. Robins, A.K. Morisson, J.J. Hope, and J.D. Close, *Phys. Rev.* **A 72**, 031606(R) (2005).
97. Y. Le Coq *et al., Phys. Rev. Lett.* **87**, 17 (2001).
98. J.-F. Riou *et al., Phys. Rev. Lett.* **96**, 070404 (2006).
99. F. Gerbier, P. Bouyer, and A. Aspect, Phys. Rev. Lett. **86**, 4729 (2001).
100. J. Fortàgh, A. Grossmann, C. Zimmermann, and T.W. Hänsch, *Phys. Rev. Lett.* **81**, 5310 (1998).
101. J. Denschlag, D. Cassetari, and J. Schmiedmayer, *Phys. Rev. Lett.* **82**, 2014 (1999).
102. D. Müller *et al.*, *Phys. Rev. Lett.* **83**, 5194 (1999).
103. L. Pruvost, D. Marescaux, O. Houde, and H. T. Duong, *Opt. Comm.* **166**, 199 (1999).
104. N.H. Dekker *et al.*, *Phys. Rev. Lett.* **84**, 1124 (2000).
105. M. Key *et al., Phys. Rev. Lett.* **84**, 1371 (2000).
106. B.K. Teo and G. Raithel, *Phys. Rev.* **A 63**, 031402 (2001).
107. P. Cren *et al., Eur. Phys. J.* **D 20**, 107 (2002).
108. K. Bongs *et al., Phys. Rev. A* **61**, R31602 (2000).
109. A.E. Leanhardt *et al.*, *Phys. Rev. Lett.* **89**, 040401 (2002).
110. Z.T. Lu *et al.*, *Phys. Rev. Lett.* **77**, 3331 (1996).
111. D. Müller, E.A. Cornell, D.Z. Anderson, and E.R.I. Abraham, *Phys. Rev.* **A 61**, 033411 (2000).
112. T. Lahaye *et al., Phys. Rev. Lett.* **93**, 093003 (2004).
113. E. Mandonnet *et al., Eur. Phys. Journ. D* **10**, 9–18 (2000).
114. P.J. Martin, B.G. Oldaker, A.H. Hiklich, and D.E. Pritchard, *Phys. Rev. Lett.* **60**, 515 (1988).
115. M. Kozuma *et al.*, *Phys. Rev. Lett.* **82**, 871 (1999).
116. S. Richard *et al.*, *cond-mat*/0303137, *Phys. Rev. Lett.* **91**, 010405 (2003).
117. M. Fauquembergue, J.-F. Riou, W. Guerin et al., *Review of Sci. Inst.* **76** (10), 103104 (2005).
118. J. Ye, S. Swartz, P. Jungner and J.L. Hall, *Opt. Lett.* **21**, 1280 (1996).
119. S. Bize, Y. Sortais, M.S. Santos, C. Mandache, A. Clairon and C. Salomon, *Europhys. Lett.* **45**, 558 (1999).
120. D. Hellweg *et al.*, *Phys. Rev. Lett.* **91**, 010406 (2003).
121. W.C. Stwalley, *Phys. Rev. Lett.* **37**, 1628 (1976); E. Tiesinga *et al.*, *Phys. Rev. A* **46**, R1167 (1992); P. Fedichev *et al.*, *Phys. Rev. Lett.* **77**, 2913 (1996).
122. M. Theis, G. Thalhammer, K. Winkler, M. Hellwig, G. Ruff, R. Grimm, and J. Hecker Denschlag, *Phys. Rev. Lett.* **93**, 123001 (2004).
123. J.L. Roberts, N.R. Claussen, S.L. Cornish, E.A. Donley, E.A. Cornell, and C.E. Wieman, *Phys. Rev. Lett.* **86**, 4211 (2001).
124. A.E. Leanhardt, T.A. Pasquini, M. Saba, A. Schirotzek, Y. Shin, D. Kielpinski, D.E. Pritchard, and W. Ketterle, *Science* **301**, 1513 (2003).
125. S. Schneider *et al., Phys. Rev.* **A 67**, 023612 (2003).
126. H. Ott, J. Fortagh, G. Schlotterbeck, A. Grossmann, and C. Zimmermann, *Phys. Rev. Lett.* **87**, 230401 (2001).
127. W. Hänsel, P. Hommelhoff, T.W. Hänsch, and J. Reichel, *Nature (London)* **413**, 498 (2001).

128. M. Vengalattore, W. Rooijakkers, and M. Prentiss, *Phys. Rev. A* **66**, 053403 (2002).
129. Y. Wang *et al., Phys. Rev. Lett.* **94**, 090405 (2005).
130. S. Gupta, Z. Hadzibabic, M.W. Zwierlein, C.A. Stan, K. Dieckmann, C.H. Schunck, E.G.M. van Kempen, B.J. Verhaar, and W. Ketterle, *Science* **300**, 1723 (2003); M.W. Zwierlein, Z. Hadzibabic, S. Gupta, and W. Ketterle, *Phys. Rev. Lett.* **91**, 250404 (2004).
131. C.A. Regal, M. Greiner, and D.S. Jin, *Phys. Rev. Lett.* **92**, 040403 (2004).
132. G. Ferrari, M. Inguscio, W. Jastrzebski, G. Modugno and G. Roati, *Phys. Rev. Lett.*, **89** 053202 (2002). F. Ferlaino, C. D'Errico, G. Roati, M. Zaccanti, M. Inguscio, and G. Modugno, arXiv:cond-mat/0510630.
133. H. Schmaljohann *et al., Appl. Phys.* **B 79**, 1001 (2004).
134. R. Nyman *et al.*, to appear in App. Phys. B. See also http://www.ice-space.fr.
135. Natural-abundance dispensers are available from SAES Getters. We are interested in the isotopes ^{87}Rb and ^{40}K, which are, respectively, 28% and 0.012% naturally abundant. We will be investing in isotopically enriched ^{40}K (about 5%) dispensers in the near future.
136. V. Mahal, A. Arie, M.A. Arbore, M.M. Fejer, *Opt. Lett.* **21**, 1217 (1996).
137. R.J. Thompson, M. Tu, D.C. Aveline, N. Lundblad, and L. Maleki, *Opt. Exp.* **11**, 1709 (2003).
138. J. Dingjan, B. Darquié, J. Beugnon, M.P.A. Jones, S. Bergamini, G. Messin, A. Browaeys, P. Grangier, *App. Phys.* **B 82**, 47 (2006).
139. C. Ospelkaus, S. Ospelkaus, K. Sengstock and K. Bongs, *Phy. Rev. Lett.* **96**, 020401 (2006).
140. T. Kinoshita, T.R. Wenger and D.S. Weiss, *Phys. Rev.* **A 71**, 01162(R) (2005).
141. Ch.J. Bordé, *Phil. Trans. Roy. Soc.* 363, 2097 (2005) and references therein.